Macrophage inflammatory and regenerative response periodicity is programmed by cell cycle and chromatin state

Bence Daniel[1,3,#*], Julia A. Belk[1,2*], Stefanie L. Meier[1,9], Andy Y. Chen,[1,8] Katalin Sandor[1], Yanyan Qi[1], Hugo Kitano[2], Joshua R. Wheeler[3], Deshka S. Foster[5,6], Michael Januszyk[5,6], Michael T. Longaker[5,6,7], Howard Y. Chang[3,4,#] and Ansuman T. Satpathy[1,#]

[1]Department of Pathology, Stanford University, Stanford, CA 94305, USA.
[2]Department of Computer Science, Stanford University, Stanford, CA 94305, USA.
[3]Center for Personal Dynamic Regulomes, Stanford University, Stanford, CA 94305, USA.
[4]Howard Hughes Medical Institute, Stanford University, Stanford, CA 94305, USA.
[5]Hagey Laboratory for Pediatric Regenerative Medicine, Division of Plastic and Reconstructive Surgery, Stanford University, Stanford, CA 94305, USA.
[6]Department of Surgery, Stanford University School of Medicine, Stanford CA 94305, USA.
[7]Institute for Stem Cell Biology and Regenerative Medicine, Stanford University School of Medicine, Stanford, CA 94305, USA.
[8]Department of Bioengineering, Stanford University, Stanford, CA 94305, USA.
[9]Parker Institute for Cancer Immunotherapy, San Francisco, CA 94129, USA.

*These authors contributed equally to this work.
#Corresponding authors

To whom correspondence should be addressed. E-mail: bdaniel8@stanford.edu, satpathy@stanford.edu or howchang@stanford.edu

Key words: cell cycle, macrophage plasticity, macrophage polarization, single-cell epigenomics

Daniel (SATPATHY)

Summary

Cell cycle (CC) is a fundamental biological process with robust, cyclical gene expression programs to facilitate cell division. In the immune system, a productive immune response requires the expansion of pathogen-responsive cell types, but whether CC also confers unique gene expression programs that inform the subsequent immunological response remains unclear. Here we demonstrate that single macrophages adopt different plasticity states in CC, which is a major source of heterogeneity in response to polarizing cytokines. Specifically, macrophage plasticity to interferon gamma (IFNG) is substantially reduced, while interleukin 4 (IL-4) can induce S-G2/M-biased gene expression. Additionally, IL-4 polarization shifts the CC-phase distribution of the population towards G2/M phase, providing a mechanism for reduced IFNG-induced repolarization. Finally, we show that macrophages express tissue remodeling genes in the S-G2/M-phases of CC, that can be also detected *in vivo* during muscle regeneration. Therefore, macrophage inflammatory and regenerative responses are gated by CC in a cyclical phase-dependent manner.

Highlights

- Single-cell chromatin maps reveal heterogeneous macrophage polarization states
- Cell cycle coincides with heterogeneity and alters macrophage plasticity to polarizing cytokines
- Macrophage polarization is a cell cycle phase-dependent immunological process
- S-G2/M-biased gene expression is linked to tissue remodeling and detected in proliferating macrophages during muscle regeneration

2

Introduction

94
95   Cellular plasticity describes the phenotypic flexibility and responsiveness of a cell
96   type in a changing microenvironment, a feature that is critical for the adaptation to
97   environmental challenges. How plasticity is established in a population of cells is a key
98   question in biology. Interestingly, certain cell types possess the ability to adopt more
99   nuanced phenotypic traits in response to stressors and can also revert from this state,
100   thus being more plastic. In the immune system, this is a particularly important cellular
101   feature, especially at the first line of defense, among the patrolling, long-lived innate
102   immune cell types of blood and tissues.
103   Macrophages (MF) are innate immune cells with remarkable plasticity. As resident
104   cell of various organs, MFs adopt distinct phenotypes to maintain tissue integrity and
105   resolve infections. They achieve this by quickly adjusting their epigenetic and gene
106   expression programs to the changing microenvironment, a phenomenon called MF
107   polarization [1-4]. In the lung, alveolar MFs respond to infections (e.g. influenza,
108   *Streptococcus Pneumoniae*) and have an important role in surfactant metabolism [4].
109   Similarly, Kupffer cells of the liver respond to pathogens but also appear to play a central
110   role in metabolizing toxic or carcinogenic compounds [5]. The pleiotropic action of MF
111   subpopulations across tissues indicate the existence of diverse MF plasticity states, tuning
112   their responses at the subpopulation level when they undergo phenotypic polarization
113   upon environmental challenges. Indeed, single-cell studies have begun to reveal MF
114   heterogeneity in multiple tissues and cancer, but no major mechanism has been offered
115   for the formation of the observed heterogeneous phenotypes, and whether certain
116   subpopulations exist in different plasticity states that would affect their polarization
117   capacity [6-8]. Importantly, a common property of MFs is their proliferative potential in the
118   tissue of residence which can be induced by MF (granulocyte) colony stimulating factors
119   (M-CSF and GM-CSF) and the T-helper 2 (Th2)-type cytokine, interleukin 4 (IL-4) resulting
120   in cell cycle (CC) entry [9-13]. MF proliferation is important to replenish the tissue resident
121   pool during both homeostatic and pathological conditions, and has been linked to the
122   resolving phase of inflammation and tissue regeneration [13-17]. However, whether CC
123   influences MF plasticity or polarization capacity has not been determined.
124   In order to uncover the phenotypic plasticity of MFs, models of classical (exposure
125   to interferon gamma (IFNG) or lipopolysaccharide (LPS) – referred to as M1 MFs) and
126   alternative (exposure to IL-4 or IL-13 – referred to as M2 MFs) MF polarization have
127   become the gold standard approach to understand the molecular principles of MF
128   responses *in vitro* [18-21]. These cellular models uncovered the remarkably dynamic
129   responses of MFs to polarizing cytokines, which can offer a direct measure of their
130   plasticity [22-25]. Although tissue environments harbor a complex molecular milieu and
131   as a result contain a spectrum of MF polarization states, these *in vitro* models proved
132   useful to mimic the most robust MF responses that can also occur *in vivo*. For example,
133   *bona fide* M1 MFs ($Nos2^+$, $Il1b^+$, Tnf^+) are present during bacterial or viral infections, while
134   M2 MFs ($Chil3^+$, $Retnla^+$, $Arg1^+$) have been observed in wound healing, helminth
135   infections, and allergic reactions [18, 19, 21]. Therefore, this model is ideal to investigate
136   MF responses to polarizing cytokines to identify fundamental mechanisms that regulate
137   plasticity and might be also translatable to *in vivo* settings.
138   MF polarization has almost exclusively been studied at the population level [22-28].
139   Therefore, our view on the transcriptomic and epigenomic programs of MF polarization is
140   hampered by the lack of sub-population level analyses. This apparent gap raises

3

141 fundamental questions about how MF plasticity is regulated at the single cell level: (1)
142 What are the major determinants of MF plasticity states? (2) Are there cell intrinsic
143 properties that influence plasticity to polarizing signals?
144   Motivated by these questions, we generated more than 30,000 single bone
145 marrow-derived macrophage transcriptomes (scRNA-seq) and *cis*-regulomes (scATAC-
146 seq) to build a comprehensive genomic atlas of IFNG-induced (M1) and IL-4-induced (M2)
147 macrophage polarization. Using this atlas, we define heterogeneous MF polarization
148 states. We report that CC coincides with heterogeneity and is a major factor that influence
149 MF plasticity during M1 and M2 polarization by sorting MFs from the different phases of
150 CC. Interestingly, MFs lose their plasticity to IFNG in the S-G2/M phases of CC, while IL-
151 4 can induce a specific gene signature at these CC-phases, correlating with phase-biased
152 enhancer activities. We find that CC negatively affects the formation of a chromatin imprint
153 that defines a subpopulation of "memory" MFs. Additionally, CC also limits MF
154 repolarization with IFNG from a M2 state. Finally, we discover a CC-intrinsic tissue
155 remodeling gene signature linked to the S-G2/M phases of CC that can be also detected
156 in proliferating MFs during muscle regeneration. Therefore, our work establishes the
157 connection between CC and MF immune responses, introducing the concept of cyclical
158 immune plasticity, which we propose to be broadly relevant to the cells of the immune
159 system.
160
161 **Results**
162 **Single-cell chromatin accessibility landscape of MF polarization**
163   In order to understand MF heterogeneity at the chromatin level, we performed
164 single-cell assay for transposase accessible chromatin using sequencing (scATAC-seq)
165 of mouse bone marrow-derived resting (unstimulated; M0; CTR), classically-polarized
166 (M1; IFNG), and alternatively-polarized MFs (M2; IL-4) **(Figure 1A)**. In total, we obtained
167 high quality scATAC-seq data from 20,275 single cells from these 3 conditions with a
168 unique fragment count above 1,000 per nuclei and a median read enrichment at
169 transcription start sites (TSSs) of >11 **(Figure S1A and S1B)**. We performed
170 dimensionality reduction using iterative latent semantic indexing (LSI) followed by UMAP
171 visualization, which revealed a clear separation between M0, M1 and M2 MF chromatin
172 states **(Figure 1B)**. Known M2 (*Arg1*) and M1 (*Cxcl9*) polarization marker genes exhibited
173 specific chromatin remodeling in the respective polarization states (quantified by Gene
174 score, see Methods), correlating with bulk gene expression levels **(Figure 1C and D)**.
175 Transcription factor (TF) footprint analysis at polarization-specific TF motifs showed
176 strong footprints at STAT6 and EGR motifs in the M2 condition, while IRF and STAT1
177 footprints were the strongest in the M1 condition, confirming our polarization model, and
178 recapitulating previously described hallmarks of MF polarization **(Figure S1C)** [23, 29,
179 30].
180   We observed a continuum of MF polarization states in the M1 and M2 conditions
181 which prompted us to assess polarization trajectories that can inform phenotypic state
182 transitions [31]. We ordered the single MF chromatin states along a vector that describes
183 the paths of the two main polarization trajectories on the UMAP. First, we reconstructed
184 the M2 polarization trajectory by the nearest-neighbor approach starting from M0 to M2
185 MFs by sequentially selecting MFs with similar chromatin states (Euclidean distances of
186 single cell chromatin states) [31, 32]. We observed the early and late chromatin
187 remodeling activities of M2 polarization, such as early chromatin closure at repressed

188 genes (e.g., *Tlr2*, *Ifitm2*, *Cd14* and *Hpgd*) and opening around "early" induced genes (e.g.,
189 *Arg1*, *Mgl2*, *Egr2* and *Klf4*) [23]. At the later points of the trajectory, we detected chromatin
190 opening around the genes of the late M2 program, including *Retnla*, *Anxa2*, *Mmp12*, and
191 *Pparg* **(Figure 1E; Table S1)** [30]. Importantly, the dynamics of chromatin remodeling at
192 specific genes over the trajectory followed their expression level from a published time
193 course bulk RNA-seq experiment [23]. This result argues that the transitional chromatin
194 states of single MFs, resulting from a 24-hour long M2 polarization can reliably recapitulate
195 the entire *cis*-regulatory/gene expression cascade of MF polarization **(Figure S1D and**
196 **S1E)**. Motif accessibility analyses over the pseudotime trajectory linked the STAT6 motif
197 to the early chromatin remodeling activities of M2 polarization, while the EGR2 motif was
198 linked to late chromatin remodeling, confirming previous findings **(Figure 1E and S1F;**
199 **Table S2)** [22, 23, 30].
200   Next, we performed the trajectory analysis of classical polarization. MF responses
201 to IFNG was more uniform; and MF chromatin states separated more clearly on the UMAP
202 with no transitional states between M0 and M1 MFs **(Figure 1F)**. The trajectory featured
203 the gene set of early chromatin closure (e.g., *Cx3cr1*, *Igf1* and *Cd14*); and early and late
204 chromatin opening, including *bona fide* IFNG-induced genes (Early - e.g., *Irf2*, *Oasl2* and
205 *Stat1*; Late - e.g., *Irf8*, *Irf5* and *Cxcl9*) **(Table S3)** [29]. Motif accessibility analysis
206 suggested the immediate early action of IRF and STAT1 motifs and decreased chromatin
207 accessibility at BACH, AP-1, RUNX and CEBP motifs over the trajectory from M0 to M1
208 states **(Figure 1F and S1F; Table S4)**. Altogether, this single cell atlas reveals the
209 transitional chromatin state program of M1 and M2 MF polarization and motivated us to
210 further investigate the chromatin structure of heterogeneous MF subsets.
211
MF heterogeneity coincides with cell cycle
213   To identify the main subpopulations of MFs, we clustered the cells and identified
214 two distinct chromatin state clusters in each condition (M0 – C5 and C6; M2 – C1 and C2;
215 M1 – C3 and C4) **(Figure 2A)**. In general, subpopulations of the polarized states did not
216 co-cluster with the clusters of the M0 state. More specifically, no M1 polarized MFs were
217 present in the M0 clusters, while approximately 10% of M2 cells remained in the M0
218 clusters (C5 and C6) **(Figure 2A)**. Next, we identified the marker gene scores of each
219 cluster (FDR$\leq$0.01, Log$_2$ fold change (FC)$\geq$1.25) **(Table S5)**. We observed C1- (n=261)
220 and C2-biased (n=113) gene scores, including several M2 marker genes in the two
221 clusters (C1 - e.g., *Retnla*, *F10*, *F7* and *Abcg1*; C2 - e.g., *Mgl2*, *Igf1*, *Ccl7* and *Ccl2*).
222 Conversely, M1 MFs exhibited C3- (n=483) and C4-biased gene scores (n=317), including
223 *bona fide* M1 marker genes in both clusters (C3 - e.g., *Gbp2*, *Gbp10*, *Ifit3*, *Cd274* and
224 *Cxcl9*; C4 - e.g., *Mmd2*, *Nlrp9b* and *Oas1c*) **(Figure 2B)**. We noticed that cell cycle (CC)
225 gene scores were largely specific to polarized M2 MFs in C2 (e.g., *Hist1h3g*) or M1 MFs
226 in C4 (e.g., *Top2a* and *Ccnf*). Importantly, the gene score values of *Mki67* aligned with the
227 CC gene scores in these clusters, indicating that MFs in C2 and C4 are engaged in CC
228 **(Figure 2C)**.
229   To link transcriptional activity to the observed chromatin changes, we performed
230 single cell RNA-seq in M0, M1 and M2 MFs, and identified the differentially expressed
231 genes between the M0 – M2 (Induced: 214, Repressed 147) and M0 – M1 (Induced: 494,
232 Repressed: 212) conditions (FDR$\leq$0.01, Log$_2$ FC$\geq$0.25) **(Figure S2A and S2B; Table**
233 **S6)**. We performed constrained integration of single cell chromatin and transcriptomic
234 profiles of the different polarization states, thereby limiting the search space and

235   enhancing the efficiency of the integrative method [32]. As a result, we generated a gene
236   integration matrix that contains pseudo scRNA-seq expression values linked to each cell
237   in the scATAC-seq space, which recapitulated our observations on cluster-biased
238   chromatin accessibility at the mRNA level **(Figure S2C)**. For example, the expression of
239   CC genes appeared to be specific to C2 of M2 and C4 of M1 polarized MFs (e.g., *Cenpt*,
240   *Top2a, Kif4* and *Cdk1*). These clusters of cells in CC (hereafter referred to as cell cycle
241   (CC)-clusters) exhibited reduced expression profiles for specific M1 (e.g., *Cxcl9* and
242   *Gbp2*) and M2 genes (e.g., *Retnla* and *Egr2*) **(Figure 2D, E and S2C)**; however, we also
243   observed genes with CC-cluster-biased expression, such as *Mgl2* in M2 polarized MFs
244   (C2) **(Figure S2C)**. Collectively, these results show that MF heterogeneity coincides with
245   CC and suggests that MF plasticity to polarization cytokines is influenced by CC.
246
247   **The *cis*-regulatory landscape of M1 and M2 MF polarization is constrained by cell**
248   **cycle**
249   After we defined the chromatin states of polarization-specific genes and their
250   expression profiles in the subpopulations of M1 and M2 MFs, we turned our attention to
251   identify the distant regulatory regions of the non-coding genome (referred to as *cis*-
252   regulatory elements - CREs). In M2 MFs we identified 916 C1-biased and 195 C2-biased
253   CREs. Analysis of M1 MFs reported 1,262 C3- and 323 C4-biased CREs (FDR $\leq$0.01,
254   Log$_2$ FC$\geq$1) **(Figure 2F)**. We observed that in both M1 and M2 MFs, cells in CC-clusters
255   (C2 and C4) showed less pronounced chromatin remodeling events upon polarization
256   compared to non-cycling cells (C1 and C3). However, we also noted a smaller set of
257   polarization-induced CREs that were biased to the CC-clusters. Motif enrichment
258   analyses at the M2-specific CREs identified the EGR2 motif in C1, while the STAT6 motif
259   showed specific enrichment in C2. In M1 MFs, we detected the STAT1 motif exclusively
260   in C3, while the IRF motif was present in both clusters but showed a more significant
261   enrichment in C3 compared to C4 (p-values: C3 - $1e^{-511}$ versus C4 - $1e^{-156}$). Single cell
262   chromatin accessibility analyses of these motifs further supported these findings **(Figure**
263   **S2D)**.
264   According to these results, the subset of non-cycling MFs showed the highest level
265   of chromatin remodeling potential in both polarization models. Interestingly, while both the
266   STAT1 and IRF motifs are largely specific to non-cycling M1 MF CREs, the binding motif
267   of STAT6 appears to show specific enrichment in the CC-cluster of M2 MFs, whereas the
268   EGR motif is specifically enriched in the non-cycling MF cluster. These results suggest
269   that STAT6 and EGR2 act in different MF subpopulations after 24 hours of IL-4
270   polarization, in agreement with a recent study that reported spatial and temporal
271   separation of the binding sites of the two TFs in M2 MFs [30]. Additionally, these results
272   imply that the main TFs of M1 (STAT1 and IRFs) and M2 (EGR2) MFs might lose some
273   of their functions in CC, but STAT6 might be able to retain its transcriptional activity.
274
275   **Cell cycle limits the expression of the two key transcription factors of MF**
276   **polarization**
277   We next asked whether CC alters the plasticity of MFs to polarization signals. First,
278   we took a predictive approach and used our gene integration matrix to assign specific CC
279   stages (G1, S and G2/M) to each cell in the scATAC-seq space using a CC scoring
280   algorithm **(Figure 3A)** [33]. This analysis showed that ~80% of the cells in C2 (M2) and
281   more than 95% of cells in C6 (M0) and C4 (M1) were in CC **(Figure S3A)**. Utilizing the

282   gene integration matrix, we performed differential gene expression analyses (FDR≤0.01,
283   FC≥1.3) between CC stages using the marker genes of M2(IL-4) and M1(IFNG) states
284   that we previously defined **(Figure S2B, Table S6)**. Comparison of G1 to G2/M yielded
285   the largest gene lists in both polarization settings, suggesting that gene expression is
286   largely biased towards the G1-phase (M1: 38 G1-biased genes; M2: 33 G1-biased genes)
287   **(Figure 3B)**. Interestingly, the M2 gene expression program showed more S- (n=6; e.g.,
288   *Atpv0d2* and *Anxa1*) and G2/M-biased (n=11; e.g., *Mgl2* and *Gatm*) genes over the G1-
289   phase as compared to the M1 program, suggesting that IL-4 might be able to initiate more
290   specific polarization programs in CC **(Figure S3B)**. The M1 program appeared to be more
291   sensitive to CC and we found a negligible number of genes with biased expression in the
292   later stages of CC (S vs. G1 – n=2; S vs. G2/M – n=1; G2/M vs. S – n=2; G2/M vs. G1 –
293   n=2). Importantly, the G1-biased gene program resulted in a largely overlapping gene set
294   from the G1-S and G1-G2/M comparisons, supporting the idea that IFNG response is
295   severely reduced in the S-G2/M phases of CC **(Figure 3B and S3B)**. Next, we examined
296   the gene sets of the G1-G2/M comparisons in the two models and found attenuated
297   expression of the typical polarization marker genes in the G2/M phase (M2(IL-4): *Anxa1*,
298   *Evl*, *Egr2*, *Atf3* and *Atp6v0a1*; M1(IFNG): *Slfn5*, *Ifit2*, *Ifit1*, *Irf8* and *Ifitm2*) **(Figure 3B)**. We
299   noticed that the TFs, *Egr2* and *Irf8* exhibited G1-biased expression and chromatin
300   accessibility profiles in M2 or M1 polarized MFs, respectively **(Figure S3C and S3D)**.
301   EGR2 is a critical regulator of M2 MF, while IRF8 orchestrates significant parts of the M1
302   MF polarization program, indicating a dysfunctional polarization program in the later
303   phases of CC [30, 34].
304   To experimentally test these observations, we used fluorescence-activated cell
305   sorting (FACS) to quantify the CC distribution of M0 MFs with a DNA labeling dye (Vybrant
306   DyeCycle) **(Figure 3C)**. This experiment reinforced the notion that MFs can be detected
307   in different CC stages, in agreement with a previous study [35]. Specifically, we detected
308   ~73% of the population in G0/G1 (referred to as G1), ~12% in S and ~6.6% in the G2/M
309   phase of CC **(Figure S3E)**. Next, we sorted F4/80$^+$ M0 MFs from the different phases of
310   CC and performed gene expression measurements by real time quantitative PCR (RT-
311   qPCR). Reassuringly, the expression of the S-phase-specific *Pold2* (DNA-polymerase
312   delta complex member required for genome replication) and the S-G2/M-specific *Mki67*
313   genes validated the purity of our sorted populations **(Figure 3D)** [36]. Then, we sorted M1
314   and M2 MFs from CC-phases and measured the expression of *Egr2* and *Irf8* by RT-qPCR,
315   which are readily induced by either IL-4 or IFNG, respectively (assessed by bulk RNA-seq
316   and RNAPIIpS2 ChIP-seq datasets) **(Figure 3E and F)** [29]. As expected, based on our
317   predictions, both *Egr2* and *Irf8* were sensitive to CC; and displayed G1-biased expression
318   in the M0 condition. Additionally, M2 polarization rapidly induced the level of *Egr2* in a G1-
319   biased manner, while M1 polarization resulted in a similar, G1-biased expression profile
320   for *Irf8* **(Figure 3E and F)**. Footprint analyses of the two TF motifs reported C1-biased
321   EGR, while C3-biased IRF footprints corresponding to non-cycling MFs, supporting the
322   gene expression results **(Figure 3E and F)**. These results might explain the dominance of G1-biased polarization programs, but also raises questions about the existence of S-
323   G2/M phase-specific polarization programs, especially in M2 MFs.
325
326   **Cell cycle phase-dependent MF plasticity influences polarization potential**
327   Next, we studied the effects of CC on MF plasticity. We performed bulk RNA-seq
328   experiments on M0, M1, and M2 MFs sorted from CC-phases. To streamline the analysis,

329 we used the top 50 polarization-induced and -repressed genes defined by our scRNA-seq
330 results **(Table S6)**, which contained the core gene expression signatures of both M1 and
331 M2 MF polarization **(Figure 4A and S4A)** [19, 21]. First, using the bulk RNA-seq results,
332 we defined CC-sensitive genes with differential expression profiles between any two CC-
333 phases in each condition, yielding a total of 8700 genes (Benjamini–Hochberg adjusted
334 p-value ≤0.001; FC≥1.3). Then we overlapped this list with our top 50 induced and
335 repressed marker genes of the two polarization models. We found that 74% of the M2
336 gene expression program was sensitive to CC (74/100 genes). Namely, 66% of the
337 induced genes and 82% of the repressed genes exhibited CC phase-dependent
338 expression. Similarly, 76% of the core M1 polarization program appeared to be CC-
339 sensitive (76/100 genes); 84% of the induced genes and 68% of the repressed genes
340 displayed CC phase-biased expression **(Figure S4B)**.
341   Next, we analyzed CC phase-biased expression among IL-4-induced genes. We
342 found genes with G1- (48%, 24/50) and S-G2/M-biased expression (18%, 9/50). In both
343 groups, we detected *bona fide* M2 MF marker genes such as the G1-biased *Retnla*,
344 *Atp6v0a1*, *Batf3*, *Hbegf* and *Egr2*, and the S-G2/M-biased *Bhlhe40*, *Fn1*, *Mgl2*, *Chil3* and
345 *Mpo* **(Figure 4B and C, Table S9)**. In contrast to the M2 program, the vast majority of
346 IFNG-induced gene expression circuit (82% - 41/50 genes) exhibited G1-biased
347 expression (e.g., *Cxcl9*, *Ifi44*, *Gbp4* and *Irf8*) and only 3 genes showed S-G2/M-biased
348 expression (*Ccl12*, *Apobec3* and *Pnp*) **(Figure S4B and C, Table S9)**. Among the 50
349 induced genes in the two polarization models, we found 17 IL-4- (e.g., *Arg1*, *Ptpre*, *Prkcd*,
350 *Gatm* and *Cblb*) and 6 IFNG-induced (e.g., *Cxcl10*, *Gbp5*, *Irf1* and *Fam26f*) but CC-
351 insensitive genes **(Figure S4F and G)**.
352   Repressed genes exhibited strong phase-biased expression in the M0 condition in
353 both polarization models. Among the IL-4 repressed genes, 62% showed G1-biased
354 expression (e.g., *Cd14*, *Ifitm2* and *Clec4d*) and 25% displayed S-G2/M-biased expression
355 (e.g., *Cx3cr1*, *Spp1* and *Ifi27l2a*) in the M0 condition. In the group of IFNG-repressed
356 genes, 44% had G1-biased expression (e.g., *Ifngr1*, *Plin2* and *C5ar1*) and 24% exhibited
357 S-G2/M-biased expression, including genes that are required for replication, in agreement
358 with the finding that IFNG triggers CC arrest at the G1-S border in MFs (e.g., *Rps28*, *Slbp*
359 and *Gmnn*) **(Figure S4E)** [37]. Therefore, repression occurs by silencing phase-biased
360 gene expression in the M0 state.
361   Due to our finding that IL-4 can specifically induce gene expression in the S-G2M-
362 phases of CC, we focused on the M2 program and validated our RNA-seq results by RT-
363 qPCR (Insensitive - *Arg1*; G1-biased - *Batf3* and *Hbegf;* S-biased - *Fn1*; G2/M-biased -
364 *Mpo* and *Chil3*) **(Figure 4D)**. Importantly, all of these genes reproduced the CC-phase-
365 biased expression patterns that we detected with RNA-seq. Collectively, our findings show
366 that the majority of the core MF polarization program is CC phase sensitive. Surprisingly,
367 IFNG-induced gene expression is strictly restricted to the G1-phase, whereas IL-4 can
368 launch specific parts of the M2 polarization program in the S-G2/M phases of CC.
369
370 **Cell cycle phase-biased expression of *Mgl2* and *Retnla* associates with phase-**
371 **biased enhancer activities**
372   Next, we set out to study the potential mechanism of phase-biased gene
373 expression. We hypothesized that phase-biased enhancers might drive gene expression
374 based on our observations of biased chromatin remodeling activities in cycling and non-
375 cycling MF clusters **(Figure 2F)**. We focused on two major components of the M2-induced

376   polarization program, *Mgl2* and *Retnla* as demonstrating either G2/M- or G1-biased IL-4-
377   induced expression patterns (RNA-seq – **Figure 4B**), respectively. Resistin-like alpha
378   (*Retnla*) is one of the most widely accepted markers of M2 polarization in both *in vitro* and
379   *in vivo* conditions. It is a secreted protein exhibiting robust induction in IL-4/-13-induced
380   M2 MFs during multicellular parasite infections (nematodes, helminths) and allergic
381   reactions. It has chemotactic activities towards eosinophils that is speculated to have roles
382   in anti-parasitic defense mechanisms [38]. Macrophage galactose-type C-type lectin
383   (*Mgl2*) is a pattern recognition receptor recognizing glycan structures and implicated in
384   antigen uptake and presentation. Importantly, *Mgl2* is also a widely known M2 marker
385   gene and is induced by Th2-type cytokines during helminth infections and asthma [39,
386   40]. First, we validated the CC-phase-biased expression of both genes, which confirmed
387   the RNA-seq results **(Figure 4E)**. Second, we inspected their genomic neighborhood,
388   searching for open chromatin regions (scATAC-seq) that align with IL-4-induced RNAPII
389   ChIP-seq signals to identify putative enhancers **(Figure 4F)**. Next, we identified CC-
390   clusters (C6 and C2), according to the clusters defined in Figure 2A and based on *Mki67*
391   accessibility. In agreement with this and the gene expression results, *Mgl2* displayed C2-
392   biased accessibility and *Retnla* showed C1-biased accessibility **(Figure 4F and H)**.

393   In the *Mgl2* locus, we identified potential enhancers with C2-biased, IL-4-induced
394   accessibility and RNAPII recruitment. Enhancer RNA (eRNA) expression is one of the
395   best markers of enhancer activity; thus, we measured eRNAs at two putative enhancers
396   located -1kb and -14kb from *Mgl2* by RT-qPCR [41, 42]. We detected G2/M-phase-
397   dependent enhancer activity in the M0 state at the -1kb enhancer, while the -14kb was
398   silent. IL-4 readily induced eRNA production at both enhancers, but the two elements
399   showed striking differences. The -1kb enhancer displayed weak IL-4-induced activity,
400   exclusively in the G2/M-phase (CTR vs IL-4 in G2/M, fold change - FC=1.56), whereas
401   the -14kb region showed strong induction upon IL-4 treatment in all phases (G1-FC=4.1,
402   S-FC=9.2) with superior G2/M-biased activity (FC=96) **(Figure 4G)**.

403   We also identified a candidate enhancer region (-11kb) at the *Retnla* locus and
404   measured enhancer activity. Although this region did not show IL-4 induced accessibility,
405   it appeared to be preferentially open in non-cycling MF clusters (C5 and C1). In addition,
406   we detected IL-4-induced RNAPII occupancy at this element. Measurement of eRNA
407   expression identified G1-biased activity in the M0 state, and IL-4 exposure robustly
408   induced eRNA production in a strongly G1-biased manner **(Figure 4G)**. These results
409   identify the putative enhancer elements that likely drive the observed CC phase-biased
410   expression of *Mgl2* and *Retnla*.

411

412   **IL-4 priming imprints a memory chromatin signature in a subpopulation of MFs and**
413   **is limited by cell cycle**
414   Our results show that MFs enter different plasticity states in a CC-phase-dependent
415   manner. Therefore, we wondered if CC might also affect other aspects of MF responses,
416   such as memory formation at the chromatin level. We used IL-4 for these experiments,
417   since this cytokine has been shown to reprogram MF responses to secondary stimuli,
418   indicative of a stable chromatin imprint [22, 23, 28]. Hence, we established a MF priming
419   model in which IL-4 polarization (24h) is followed by cytokine washout and resting (24h –
420   IL-4-primed; referred to as M2p) and performed scATAC-seq **(Figure 5A)**. Dimensionality
421   reduction followed by UMAP of the M0, M2, and M2p MFs (n=18,376) suggested that the
422   chromatin structure of M2 MFs is not stable after the removal of IL-4. Notably, the majority

423 (~95%) of the cells from the M2p condition did not colocalize with either the M2, or the M0
424 states, suggesting a largely transient IL-4-induced chromatin imprint but also indicating a
425 unique chromatin structure of primed MFs **(Figure 5B)**.
426   Clustering MFs based on their chromatin states resulted in 6 clusters (M0 – C5 and
427 C6; M2 – C1 and C2; M2p – C3 and C4). Among these, C2, C4 and C6 showed high
428 *Mki67* accessibility, which reliably identifies cycling cells (Figure 3A), thus we designated
429 them as CC-clusters **(Figure 5C)**. Identification of the specific CREs of the clusters
430 revealed that the majority of IL-4-induced chromatin changes are lost after the removal of
431 the cytokine, but cells in the primed state displayed a specific CRE program (C3 and C4)
432 (FDR ≤0.01, Log$_2$ FC≥1) **(Figure S5B)**. Notably, we found 1,641 IL-4-induced CREs, of
433 which 1,530 returned to the steady state ("Transient") and 111 showed persistent
434 accessibility following IL-4-washout ("Memory"). We also observed 689 CREs that
435 exhibited induced accessibility following IL-4-washout ("Primed") **(Figure 5D, Table S7)**.
436 As expected, these groups of CREs followed the anticipated accessibility patterns along
437 the trajectory of priming by connecting and studying the transitional chromatin states of
438 the 3 conditions (M0 – M2 – M2p) **(Figure 5E and S5A)**. Importantly, the accessibility of
439 the "Transient" and "Primed" CREs were impacted in the CC-clusters. Specifically, 233
440 (C1-biased) and 21 (C2-biased) of the "Transient" CREs showed either reduced or
441 increased accessibility in CC, respectively. Among the "Primed" CREs, 85 (C3-biased)
442 and 8 (C4-biased) were either reduced on increased in CC, respectively **(Figure S5B)**.
443 CREs with "Memory" characteristics followed a similar trend and showed 36 (C1-biased)
444 and 13 (C2-biased) genomic regions with either reduced or increased accessibility in CC,
445 respectively. We calculated the median peak score values of the "Memory" CREs in each
446 cluster and found that both the establishment (comparing C1 to C2) and stability
447 (comparing C3 to C4) of this chromatin imprint was negatively affected by CC (Wilcoxon
448 Signed Rank Test, p<0.0001) **(Figure 5F)**. Finally, we annotated the CREs from the 3
449 groups to their putative target genes based on co-accessibility (see Methods) and
450 proximity (200kb window around the gene TSS, **Table S7**). As expected, annotated genes
451 also featured similar chromatin remodeling dynamics as the annotated CREs as judged
452 by their gene score values (e.g., *Arg1* – "Transient", *F7* – "Memory", *Atp6v0d2* – "Primed")
453 **(Figure 5G)**.
454   Lastly, we identified genes exhibiting cluster-biased chromatin accessibility in the
455 context of priming (FDR ≤0.01, Log$_2$ FC≥1.25). We focused on the ones that displayed
456 C1- (non-cycling) or C2-biased (CC-cluster) accessibility scores from the M2 polarized
457 condition to identify IL-4-induced chromatin remodeling events. As a result, we found 102
458 genes with C1- and 85 genes with C2-biased accessibility **(Figure S5C)**. Visualization of
459 the top 30 gene scores showed that C1-biased genes are strongly induced by IL-4
460 polarization and their accessibility is preferentially retained in C3 (non-cycling) of the
461 primed cells **(Figure 5H)**. Furthermore, several of these genes had annotated memory
462 CREs in their proximity (e.g., *Epha1*, *F10* and *Atp6v0a1*) **(Figure 5H)**. In contrast, the top
463 30 genes with C2-biased accessibility demonstrated strong CC-induced chromatin
464 remodeling events, including CC-genes (e.g., *Top2a* and *Tubb5*), and IL-4 had effects on
465 only 50% of the genes (e.g., *Clec10a* and *Rnase2a*) **(Figure S5D)**. Altogether, our results
466 identify "Transient", "Memory" and "Primed" CREs. CC negatively affects the
467 establishment of the majority of CREs in these groups, including the memory chromatin
468 imprint in a subset of IL-4-primed MFs. Therefore, CC limits chromatin remodeling events

469 during MF priming with IL-4, providing an additional example of CC-influenced MF
470 response.
471
472 **IL-4 priming and cell cycle limits repolarization by IFNG at the chromatin level**
473 After we provided multiple lines of evidence that CC affects MF plasticity during
474 M1/M2-polarization and priming, we set out to study an additional widely used system to
475 test MF plasticity, called repolarization. In the experimental setting of repolarization, MFs
476 are first polarized with either an M1 or an M2 cytokine followed by the treatment of the
477 opposing polarization signal to assess the plasticity of the underlying polarized state [20,
478 23]. To study repolarization capacity, we performed IL-4-priming according as previously
479 described **(Figure 5A)**, but after the resting period we exposed the cells to IFNG for 3
480 hours (repolarization) and performed scATAC- and scRNA-seq **(Figure 6A)**. Using the
481 single cell chromatin maps, we projected our 4 conditions (M0, M2p, M1 and repolarized
482 – M1rep(pIL-4+IFNG)) and observed that the M1rep cells clustered close to the M1
483 polarized cells but only slightly overlapped with this condition on the UMAP **(Figure 6B)**.
484 We identified 2 clusters in each condition (8 clusters total) **(Figure 6C)**. Importantly, one
485 of the 2 identified clusters in each condition were CC-clusters exhibiting strong
486 accessibility for CC genes (C1 – M1; C4 – M1rep; C5 – M0 and C8 – M2p), such as *Top2a*,
487 *Ccnf*, *Hist1h2bb* and *Mki67* **(Figure 6D and S6A)**, further reinforced by the expression
488 (gene integration score) of *Mki67* **(Figure S6B)**.
489 Next, we defined the IFNG-induced chromatin remodeling events that are free from
490 the effects of CC, using non-cycling M1 MFs from C2 **(Figure 6C, D)**. We identified 234
491 marker genes in C2 and found that these genes exhibited significantly weaker accessibility
492 in the M1 MF CC-cluster (C1) (FDR $\leq$0.01, Log_2 FC$\geq$1), reinforcing our RNA-seq results
493 **(Table S8)**. Interestingly, we also detected reduced accessibility of these genes in non-
494 cycling M1rep MFs in C3, suggesting that IL-4-priming has a similar effect on the
495 chromatin state of these genes as CC. Furthermore, MFs in C4 (M1rep MFs in the CC-
496 cluster) displayed an even more severe defect in chromatin remodeling upon IFNG
497 stimulation, suggesting that CC and IL-4-priming shift this subpopulation into an "IFNG-
498 tolerant" plasticity state **(Figure 6C and E)**. To link these findings with the RNA-seq results
499 of CC-phase sorted MFs, we overlapped the IFNG-induced, G1-biased gene signature
500 (Figure S4D; 41 genes) with the marker gene scores of C2. This yielded a list of genes
501 that are negatively affected by CC at both the gene expression and chromatin level, while
502 IL-4 priming also reduced their sensitivity to IFNG at the chromatin level (n=19; e.g., *Fcgr3*,
503 *Cxcl9*, *Fcgr4*, and *Irf8*) **(Figure 6F)**. These results indicate that IL-4-priming and CC might
504 work in an additive or even in a synergistic fashion to further reduce MF plasticity to IFNG
505 at the subpopulation level.
506 We tested this hypothesis on three IFNG-induced genes, two of which are CC-
507 sensitive, *Cxcl9* and *Irf8*; and one that is CC-insensitive, *Cxcl10* (as revealed by RNA-
508 seq). First, we performed RNAPII ChIP-seq in the repolarization system. Second, we
509 visualized aggregated scATAC-seq with the RNAPII ChIP-seq signal from M0, M1, M2p
510 and M1rep conditions on the loci of *Cxcl9* and *Cxcl10* **(Figure 6G)**. As expected, IFNG-
511 induced chromatin remodeling and RNAPII recruitment was reduced in the M1rep
512 condition compared to the M1 state. Importantly, the two gene loci appeared to behave
513 essentially the same in the bulk datasets. However, when we visualized the scATAC-seq
514 signal in each cluster, we observed striking differences. *Cxcl9* exhibited reduced
515 accessibility in cycling, M1 polarized cells (C1) and also after IL-4 priming in non-cycling

516 cells (C3). We detected an even lower level of accessibility in IL-4-primed, cycling MFs
517 (C4) **(Figure 6G and S6A)**. In addition to this, we observed similar chromatin accessibility
518 changes around *Irf8* **(Figure S6A)**. In contrast, *Cxcl10* did not show differences between
519 cycling (C1) and non-cycling (C2) M1 polarized MFs. Moreover, we detected uniformly
520 reduced chromatin accessibility in both cycling (C4) and non-cycling (C3) M1rep MFs
521 **(Figure 6G)**. Gene integration scores from the scRNA-seq experiments also supported
522 these observations on all of these genes **(Figure S6B)**.
523   In order to provide experimental evidence that CC and IL-4-priming can limit IFNG
524 responsiveness at the subpopulation level, we measured gene expression from CC phase
525 sorted MFs from M0, M1 and M1rep conditions. *Cxcl9* and *Irf8* exhibited reduced
526 expression levels in the S and G2/M phases of CC upon IFNG treatment validating the
527 bulk RNA-seq results. However, we detected greater reduction of the IFNG response in
528 the S and G2/M phases of CC from M1rep MFs, confirming our previous results that CC
529 and IL-4-priming are two major factors that can limit MF plasticity to IFNG. Moreover, CC
530 and priming appeared to reduce IFNG response in a synergistic or additive fashion on
531 *Cxcl9*, or *Irf8*, respectively. In contrast, *Cxcl10* was not sensitive to CC, and IL-4-priming
532 uniformly reduced MF plasticity to IFNG in all CC-phases **(Figure 6H)**.
533   Since IL-4 has been described to induce MF proliferation *in vivo*, we wondered if
534 the M2 and M2p MF populations display differences in their CC-phase distribution, which
535 can provide an additional mechanism to limit IFNG responsiveness according to our
536 previous results [38]. Using FACS, we quantified the CC-phase distribution of M2 and M2p
537 MF populations and have not detected significant differences in the G1- or S-phase but
538 observed a 35% increase in MF numbers in the G2/M-phase of CC **(Figure 6I and S6D)**.
539 Therefore, our results provide strong evidence that MF plasticity to IFNG is reduced in
540 CC, and IL-4 priming achieves very similar effects in non-cycling cells. Surprisingly,
541 plasticity to IFNG has dramatically changed in cycling, M2p MFs, suggesting that priming
542 with IL-4 and CC are two major and complimentary factors that can affect MF plasticity at
543 the subpopulation level. Furthermore, IL-4 can change the CC-phase distribution of the
544 population, directing more MFs into the G2/M-phase, representing an additional
545 mechanism to limit IFNG response at the population level.
546
547 **MFs express a cell cycle-intrinsic tissue remodeling gene program**
548   Our findings show that CC determines the plasticity of MFs to environmental
549 changes (i.e., polarization signals) but whether there are CC-intrinsic gene expression
550 programs which might support specialized macrophage functions is unknown. Therefore,
551 we sought to study the gene expression program of CC-phase sorted (G1, S and G2/M)
552 M0 macrophages by RNA-seq. Differential gene expression analysis of a three-way
553 comparison across the CC-phases identified 3,776 CC-sensitive and 7,327 insensitive
554 genes (Benjamini–Hochberg adjusted p-value ≤0.001; FC≥1.3) **(Figure 7A and S7A)**. We
555 performed pathway analysis on the CC-sensitive genes, which showed CC-related
556 functional categories, including "Kinetochore metaphase signaling pathway" and "Cell
557 cycle control of chromosomal replication". Surprisingly, we also noted functional terms
558 that are related to fibrosis and tissue remodeling, for example, "Hepatic fibrosis/Tissue
559 remodeling" **(Figure 7B)**. As expected, the first two terms mainly described the known
560 gene expression program of the S (e.g., *Pcna*, *Mcm2* and *Pola1*) and G2/M (e.g., *Cenpp*,
561 *Cenpe* and *Spdl1*) phases of CC **(Figure 7C)**. However, genes in the fibrosis and tissue
562 remodeling term also exhibited S-G2/M-phase-biased expression (*Mmp9*, *Col1a1*,

563 *Col1a2*, *Acta2*, *Fn1* and *Vcam1*). We sorted MFs and validated the CC phase-dependent
564 induction of *Fn1*, *Acta2* and *Col1a1*, reproducing the RNA-seq results **(Figure 7D)**.
565 Collectively, these results uncover a CC-intrinsic gene expression signature that is linked
566 to tissue remodeling and fibrosis, preferentially expressed in the S-G2/M phases of CC.
567 Interestingly, these genes are linked to tissue regeneration in different model systems of
568 wound healing and muscle regeneration after injury, suggesting the potential relevance of
569 cycling MFs during *in vivo* conditions [16, 28]. Additionally, MF proliferation has been
570 noted as a feature of the resolving phases of inflammatory processes and regeneration,
571 raising the question whether proliferating MFs can express the uncovered tissue
572 remodeling genes under *in vivo* circumstances [14, 16, 17].
573
574 **Proliferating MFs express tissue remodeling factors during tissue regeneration**
575   MFs are indispensable for proper muscle regeneration [44-46]. We reanalyzed
576 single cell transcriptomic datasets of regenerating muscle, which exhibits monocyte - MF
577 differentiation in the inflammatory phase and MF proliferation in the regenerative phase.
578 Importantly, in the regenerative phase, MFs can support angiogenesis and extracellular
579 matrix remodeling, which is required for regeneration [15, 16]. We processed a dataset of
580 cardiotoxin (CTX)-induced muscle injury of the *tibialis anterior* muscle of mice, where
581 regeneration was followed at 7 different time points until day 21 (days 0, 0.5, 2, 3.5, 5, 10
582 and 21) [47]. We subset MFs based on the expression of *Adgre1* (F4/80), *Mrc1*, *Msr1* and
583 *Itgam* (LogNorm.Expression>0.5); and found 5,997 cells exhibiting the combinations of
584 these features. We observed a massive surge in MF numbers starting at day 2 (n=537
585 versus day 0.5 n=15), that peaked at day 3.5 (n=3,655) and began to decline at day 5
586 (1,586). By days 10 (n=134) and 21 (n=68), MF count almost returned to the baseline,
587 where damaged myofibers are regenerated (days post injury - DPI10) and the tissue is
588 fully restored (DPI21), respectively **(Figure S7B)** [36]. Due to these temporal patterns in
589 MF numbers, we subset MFs from days 2, 3.5 and 5 following the injury (n=5,778) and
590 performed dimensionality reduction **(Figure 7E)**. MFs did not cluster based on CC, but
591 rather, cycling cells appeared to be scattered in the low dimensional space between the
592 different MF phenotypes based on CC-scoring and the expression of CC genes (*Pcna*,
593 *Mki67* and *Cenpa*) **(Figure S7C)**. We detected more cells expressing these CC genes at
594 days 3.5 and 5 compared to day 2 in line with our observations on the overall MF numbers
595 observed at these days. Additionally, we found 4 of the 6 tissue regeneration genes also
596 followed this expression pattern (*Acta2*, *Fn1*, *Col1a1* and *Col1a2*) **(Figure 7F)**. Next, we
597 focused on MFs that express both the CC and the tissue remodeling genes
598 (LogNorm.Expression>0.1); and performed a correlation analysis. We observed positive
599 correlation between the expression of the collagen genes (*Col1a1* and *Col1a2*) and all
600 three CC genes at the single cell level **(Figure 7G)**. Additionally, we found positive
601 correlation between *Pcna – Acta2* and *Pcna – Fn1* expression supporting the finding that
602 proliferating M0 MFs express this gene set. Although there was no correlation between
603 either *Cenpa - Acta2* or *Cenpa - Fn1*, nor between *Mki67 - Acta2* or *Mki67 - Fn1* providing
604 an internal negative control showing that the expression level of these genes in single
605 MFs that express these genes are not always correlated **(Figure S7D)**.
606   Next, we analyzed another muscle regeneration dataset, in which regeneration was
607 studied after barium chloride-induced *tibialis anterior* injury at days 4 and 7 after the
608 challenge [48]. We subset MFs by the expression of *Mrc1*, *Msr1*, *Itgam* and *Adgre1*
609 (LogNorm.Expression>0.5), performed dimensionality reduction and identified 5 clusters

610 **(Figure S7E and S7F)**. In cluster 2, MFs expressed CC genes (*Mcm6*, *Pcna*, *Mki67* and
611 *Cenpa*) along with tissue remodeling genes (*Fn1*, *Mmp9*, *Col1a1* and *Col1a2)* **(Figure**
612 **S7G and S7H)**. We performed correlation analyses using MFs that co-express the CC
613 markers and the collagen genes. Importantly, the collagen genes also showed positive
614 correlation with all three CC-genes in this system as well **(Figure S7I)**.
615   Finally, we used a spatial transcriptomics dataset of a stented wound healing
616 mouse model [49]. In this system, a stent is introduced into the dorsal skin of mice that
617 more closely mimics human wound healing kinetics by disrupting the immediate wound
618 construction mechanism achieved by the subdermal muscle layer called *panniculus*
619 *carnosus*. After an incision is made, healing of the wound can be studied by collecting
620 tissue sections for spatial transcriptomics **(Figure S7J)**. We utilized uninjured and injured
621 (7 days post operation) spatial transcriptomic profiles generated by the 10x Genomics
622 Visium platform. Clustering the tissue sections according to the transcriptional programs
623 of each Visium spot yielded 7 clusters. Three of these clusters (1, 7 and 3) exhibited high
624 expression of MF markers, which were virtually absent in the uninjured state (*Msr1*, *Mrc1*
625 and *Spi1*) **(Figure 7H)**. We observed massive MF infiltration at the center of the injury site
626 as noted previously, mainly corresponding to cluster 1 and 7 [38]. Interestingly, cluster 7
627 showed high expression for both *Mki67* and the MF marker genes. This same region in
628 the dermis exhibited the highest expression of the tissue regeneration-related genes (*Fn1*,
629 *Col1a1*, *Acta2*, *Col1a2*, *Mmp9* and *Vcam1*), where both MFs and fibroblasts can produce
630 these gene products **(Figure 7H and S7F)**. In summary, our results reveal the expression
631 of a CC-intrinsic tissue remodeling gene signature, which is preferentially expressed in
632 the S-G2/M-phases of CC in M0 MFs. These muscle regeneration and wound healing
633 models provide evidence that cycling MFs can express parts of this signature *in vivo*.
634
635 **Discussion**
636   MFs exist in distinct plasticity states within tissues, and the overall heterogeneity of
637 the population can be decisive when environmental factors perturb the homeostatic
638 balance, for example in the presence of infection, injury, or cancer [50, 51]. Understanding
639 the drivers of heterogeneity is of great interest due to the programmability of the MF niche,
640 but the major determinants are still unknown. Here we provide evidence that one of the
641 most fundamental biological processes, CC, influences MF plasticity.
642   MF proliferation is a general phenomenon across tissues during an immune
643 challenge [17, 38, 52, 53]. Entering CC replenishes and maintains MF populations,
644 although progression through the phases of CC can provide opportunities to support
645 additional immunological functions, a concept that has not been covered. We coin the
646 term, cyclical immune plasticity, which describes MF plasticity to polarization signals and
647 immunological functions in the different phases of CC. We provide evidence for CC-
648 impacted MF responses in three independent model systems: 1. polarization; 2. priming;
649 and 3. repolarization.
650   In the MF polarization model, scATAC- and scRNA-seq uncovered heterogeneous
651 responses to polarization cues, which coincided with CC markers. Single cell studies
652 typically regress out CC effects that can strongly bias the clustering of immune cell
653 populations. As a result, in these studies, CC-associated phenotypic traits remain hidden
654 [54]. Here, we exploited this feature of our datasets to assess MF plasticity in CC.
655 Importantly, we provide experimental evidence that MFs launch biased polarization
656 programs in the different phases of CC, using two of the main polarization signals (IL-4

657 and IFNG). MF polarization by these and many other cytokines have been extensively
658 studied, yet these studies have not implicated CC as a factor that can alter MF plasticity
659 or immune functions [22, 23, 26, 27, 29, 55]. Strikingly, we report that the M1 polarization
660 program is strongly restricted to the G1-phase of CC. In fact, IFNG and LPS triggered M1
661 polarization has been reported to arrest MFs in G1 or at the border of G1-S transition,
662 perhaps to support the completion of the polarization process in agreement with our
663 findings [37]. In contrast, although ~50% of the IL-4-induced gene expression program is
664 also G1-biased, a significant part of M2 polarization occurs in a S-G2/M-biased fashion,
665 including *bona fide* polarization marker genes, such as *Chil3*, *Mgl2* and *Fn1*. Moreover,
666 we provide evidence that these gene expression patterns are carried out by phase-biased
667 enhancer activities. Considering that IL-4 can induce MF proliferation *in vivo*, we propose
668 that CC entry in conjunction with the IL-4-induced, phase-biased transcriptional programs
669 might synergize to achieve heterogeneous polarization states that are collectively known
670 as the "M2 polarized" phenotype at the population level [12, 13, 38].
671 MFs are notoriously one of the most plastic immune cell types [1, 2]. We tested this
672 feature in an IL-4 priming model by performing polarization, cytokine washout, and rest.
673 This system allowed us to study the transient and stable chromatin states of MFs.
674 Population-level analysis of the chromatin states of MF polarization revealed mostly
675 transient chromatin remodeling events after the removal of polarization signals, although
676 stability has been also noted [22, 23, 28, 43]. Our single cell chromatin accessibility map
677 in the priming model recapitulated the transient nature of the polarization process but
678 identified a subset of "memory" MFs. This MF subset retained an IL-4-induced chromatin
679 imprint around a specific set of polarization marker genes after cytokine removal.
680 Importantly, we show that the memory imprint is sensitive to CC, thus cycling MFs cannot
681 efficiently establish this chromatin state.
682 Several studies have employed opposing polarization signals and repolarization
683 from a polarized state to mimic MF responses in complex immunological
684 microenvironments [23, 28, 29]. These studies used bulk epigenome-mapping
685 technologies and explained differences in MF responses solely by epigenetic effects that
686 were established by the first stimuli, without providing single cell insights. Our
687 repolarization model of M2 MFs with IFNG sheds light on a dampened inflammatory
688 response, where CC and IL-4 priming work together to limit MF plasticity to IFNG at the
689 subpopulation level. These findings provide further evidence for the roles of CC in shaping
690 MF plasticity, and our results confirm that IL-4 priming can skew the CC-phase distribution
691 of the population towards the G2/M-phase. Hence, MFs enter a highly restrictive plasticity
692 state, not permissive to IFNG-induced transcription, which can also limit repolarization at
693 the population level.
694 MF presence and proliferation is an apparent feature of regenerating tissues after
695 injury or infections [14, 15, 16, 17]. Recent studies already noted the uncoupling of MF
696 inflammatory and proliferative responses during infections of the lung and liver,
697 connecting MF proliferation to the resolution of inflammation and regeneration [14, 17]. In
698 agreement with this, our results indicate that MFs are less responsive to IFNG, while gain
699 tissue remodeling gene expression programs in CC. Therefore, we propose that CC entry
700 might provide a cyclical mechanism to dampen inflammation and support regeneration.
701 Using published scRNA-seq datasets of regenerating muscle, we identified proliferating
702 MF subsets, where the expression of tissue remodeling genes (*Col1a1* and *Col1a2*) and
703 CC genes displayed positive correlation at the single cell level [47, 48]. Furthermore,

704   spatial transcriptomics of wound healing also supported this concept, by defining a tissue
705   layer of high MF-specific gene expression, along with the expression of the tissue
706   remodeling gene set and *Mki67* [49]. These results imply that MFs not only change their
707   plasticity states in the phases of CC but might also gain CC phase-intrinsic transcriptional
708   programs, other than the ones that support DNA replication and cell division. Therefore,
709   our findings are not only compatible with the growing recognition that MF proliferation
710   aligns with the reparative phase of tissue injury and resolution of inflammation, but also
711   puts forward the idea that MFs might obtain tissue regeneration-linked genetic programs
712   in CC [14, 16, 17].
713   In summary, our results allow us to formulate the concept of cyclical immune
714   plasticity using a model system of MF polarization. We propose that additional cell types
715   of the immune system might use CC entry not only to replenish cell populations but also
716   to tune their phenotype and level of plasticity, increasing cellular heterogeneity and
717   flexibility at the population level. Future single cell studies should investigate and consider
718   the role of CC as an immune regulatory process during infections and cancer. Finally, anti-
719   cancer therapeutic applications targeting CC (e.g., CDK4/6 inhibitors) should be re-
720   evaluated with respect to the immune cell community of the tumor microenvironment to
721   understand how CC inhibition affects immune cell function [45].
722
723   **Limitations of the study**
724   Although our results provide a few specific cases of CC phase-biased gene/enhancer
725   activities, a more in-depth mechanistic understanding of CC-phase-biased gene
726   expression is required. Additionally, identifying the TFs that drive phase-biased
727   expression will be important future work for both the polarization-induced and the S-G2/M-
728   intrinsic tissue remodeling gene set. Another caveat is the lack of knowledge on the
729   mechanism by which IL-4 priming, and CC obtain similar, negative effects on MF IFNG
730   response. We speculate that a still ongoing M2- or CC-driven gene expression programs
731   might dampen MF plasticity to IFNG stimulation by squelching the basic transcriptional
732   machinery and lowering the cells' energy supply. Finally, although we use three different
733   tissue regeneration models to provide correlative evidence for the appearance of the
734   tissue remodeling gene set in cycling MFs *in vivo*, additional experiments will need to
735   directly assess MF CC and its importance in tissue regeneration.
736

751 1F32CA239312-01A1 (D.S.F), the Advanced Residency Training at Stanford (ARTS)
752 program (D.S.F.). NIH 1R01GM116892 (M.T.L), NIH 1R01GM136659 (M.T.L).
753

Author contributions:
755 B.D., H.Y.C and A.T.S conceptualized the study. B.D., J.A.B., H.Y.C., and A.T.S. wrote
756 and edited the manuscript and all authors reviewed and provided comments on the
757 manuscript. B.D., K.S., and Y.Q. performed experiments. J.A.B., S.L.M., A.Y.C., J.R.W.,
758 and H.K. analyzed data. B.D., H.Y.C. and A.T.S. guided experiments and data analysis.
759 D.S.F., M.J., J.R.W., and M.T.L. performed analyses and provided single cell and spatial
760 transcriptomics datasets.
761

Declaration of interests:
763 J.A.B. is a consultant for Immunai. A.T.S. is a founder of Immunai and Cartography
764 Biosciences and receives research funding from Allogene Therapeutics and Arsenal
765 Biosciences. H.Y.C. is a co-founder of Accent Therapeutics, Boundless Bio and
766 Cartography Biosciences, and an advisor to 10x Genomics, Arsenal Biosciences, and
767 Spring Discovery.
768

Data availability:
770 Sequencing data has been deposited to GEO under accession: GSE178526
771 Published data that has been used in this study: GSE138826, GSE84520.

772

Figure Legends

774

Figure 1. Single cell cis-regulatory program identifies heterogeneous macrophage subsets during polarization.
777 **(A)** Schematic of the experimental system used. **(B)** UMAP projection of scATAC-seq
778 results on polarized macrophages. **(C)** UMAP projection of gene score (accessibility)
779 values for *Arg1* and *Cxcl9*. **(D)** Genome browser views of scATAC-seq results in bulk on
780 the *Arg1* and *Cxcl9* loci (top). Bulk gene score values of CTR (red), IFNG (blue) and IL-4
781 (green) polarized macrophages for *Arg1* and *Cxcl9* along with their mRNA levels as
782 determined by RT-qPCR (bottom). **(E)** UMAP projection of the alternative polarization
783 trajectory on the M0(CTR) – M2(IL-4) transitional states (left). Heatmap of gene scores
784 changing over the polarization trajectory. Genes that lose- (Lost - blue), gain early- (Early
785 - green), or late (Late - red) accessibility are marked and a select set is displayed. *Tlr2*,
786 *Arg1* and *Itgax* gene scores are shown over the pseudotime. ChromVAR transcription
787 factor motif deviation scores over pseudotime on the alternative polarization trajectory. **(F)**
788 Same as panel E; for the Classical polarization trajectory that describes the transitional
789 states between M0(CTR) – M1(IFNG).

790

Figure 2. Macrophage heterogeneity coincides with cell cycle markers.
792 **(A)** scATAC UMAP of macrophage polarization colored by the 6 macrophage clusters.
793 Percentage-wise distribution of the clusters across the M0(CTR), M1(IFNG) and M2(IL-4)
794 samples (bottom). **(B)** Heatmap representation of a select set of marker gene scores in
795 the clusters of either M2(IL-4) or M1(IFNG) macrophages. **(C)** UMAP of *Mki67* gene
796 scores. Violin plot of *Mki67* gene scores in the clusters. **(D)** Bar graphs depict bulk mRNA

797 levels of *Retnla* and *Cxcl9* (left). UMAPs and violin plots show the gene score values (log$_2$
798 normalized counts+1) (scATAC-seq) for the two genes (middle). UMAPs of gene
799 integration scores (gene expression - scRNA-seq), # - normalized. **(E)** Genome browser
800 views of scATAC-seq signal in the 6 clusters on the *Retnla* and *Cxcl9* loci. **(F)** Peak score
801 heatmap of differentially accessible cis-regulatory regions in the clusters (top). Homer *de*
802 *novo* motif search results on the cluster-specific peaks. The number of regions in each
803 cluster and the p-values for the enriched motifs are shown (bottom).

805 **Figure 3. Cell cycle limits the expression of Egr2 and Irf8 during polarization.**
806 **(A)** UMAP of cell cycle scores in the polarized macrophage populations. **(B)** Differential
807 gene expression analysis of G1 and G2/M predicted cells from the polarized states
808 (scheme). Heatmap of genes exhibiting G1-biased expression in M2(IL-4) (left) or
809 M1(IFNG) (right). *Egr2* and *Irf8* transcription factors are marked by red asterisks and their
810 bulk expression level is validated by RT-qPCR. **(C)** Scheme of cell cycle sorting. **(D)**
811 mRNA levels of *Pold3* and *Mki67* measured by RT-qPCR in cell cycle phase-sorted
812 macrophages. **(E)** Genome browser view of bulk RNA-seq and RNAPII ChIP-seq results
813 on the *Egr2* locus in M0(CTR) and M2(IL-4) macrophages. mRNA level of *Egr2* in cell
814 cycle phases, significant changes were determined by two tailed, unpaired t-test at p<0.05
815 (n=3). Shown are means with SDs. EGR transcription factor footprints in the 6 scATAC
816 clusters. **(F)** Same as panel E; for *Irf8.*

818 **Figure 4. Cell cycle phase specifies macrophage plasticity to polarization signals.**
819 **(A)** Volcano plot of the top 50 differentially expressed gene upon M2(IL-4) polarization
820 determined by scRNA-seq. **(B)** Heatmap of cell cycle phase sensitive, IL-4-induced genes
821 determined by bulk RNA-seq. **(C)** Genome browser snapshots on a select set of genes
822 exhibiting phase-biased expression. **(D)** Validation of cell cycle phase-biased gene
823 expression by RT-qPCR. **(E)** Validation of the phase-biased expression of *Mgl2* and
824 *Retnla* by RT-qPCR. **(F)** Genome browser views on the *Mgl2* and *Retnla* loci showing
825 scATAC-seq signal in the clusters of M0(CTR) and M2(IL-4) macrophages along with bulk
826 RNAPII ChIP-seq results in the same conditions. **(G)** Enhancer RNA measurements by
827 RT-qPCR on the *Mgl2* and *Retnla* loci. **(H)** Violin plots depict the gene score values of
828 *Mki67*, *Mgl2* and *Retnla* in the 4 clusters of M0(CTR) and M2(IL-4) macrophages.
829 On the bar graphs, significant changes were determined by two tailed, unpaired t-test at
830 p<0.05 (n=3). Shown are means with SDs.

832 **Figure 5. Cell cycle negatively affects the formation of memory in a subset of**
833 **macrophages at the chromatin level.**
834 **(A)** Scheme on the model of M2 polarization and priming (M2p). **(B)** UMAP of M0(CTR),
835 M2(IL-4) and the primed M2p(pIL-4) macrophage states. **(C)** UMAP colored by the 6
836 clusters identified. Violin plot depicts the gene score of *Mki67* in the 6 clusters. Cell cycle
837 icons highlight clusters of cells predicted to be in cell cycle. **(D)** Upset plot of the
838 differentially accessible cis-elements in M0(CTR) vs. M2p(pIL-4) and M0(CTR) vs. M2(IL-
839 4) comparisons, and their overlap, yielding "memory", "primed" and "transient" chromatin
840 features (cis-regulatory elements). Scheme represents the behavior of these chromatin
841 features across the conditions. **(E)** Heatmap of peak scores exhibiting distinct chromatin
842 remodeling dynamics over the pseudotime of M2 polarization and priming. 25 peaks are
843 shown **(F)** Heatmap visualization of the "Memory" peak scores from panel D across the 6

844   clusters. Peaks with significantly biased accessibility scores are highlighted in C1 and C2.
845   Violin plot representation of the distribution of peak scores across the clusters (bottom).
846   Wilcoxon Signed Rank Test, p<0.0001. **(G)** UMAP visualization of the gene score values
847   for the indicated genes that display different chromatin remodeling activities in the 3
848   conditions (left). Genome browser views of scATAC-seq signal from the 6 clusters on the
849   indicated gene loci (right). **(H)** Heatmap of cluster 1 marker gene scores (top30) over all
850   clusters (left). Genome browser views of scATAC-seq signal from the 6 clusters on the
851   indicated gene loci (right). Cell cycle icons highlight clusters of cells predicted to be in cell
852   cycle.
853

854   **Figure 6. IL-4 priming cooperates with cell cycle to limit the repolarization capacity**
855   **of IFNG in a subset of macrophages.**
856   **(A)** Scheme on the model of IL-4 priming and repolarization by IFNG. **(B)** UMAP of
857   M0(CTR), M2p(pIL-4) – IL-4-primed, M1(IFNG) and M2repol(pIL-4+IFNG) – IL-4-primed
858   and repolarized with IFNG conditions. **(C)** UMAP colored by the 8 chromatin clusters.
859   Clusters of cells predicted to be in cell cycle are indicated with cell cycle icons. **(D)**
860   Heatmap of cell cycle marker gene scores. UMAP of *Mki67* gene score values. Log$_2$
861   normalized counts+1 is shown. Genome browser snapshot of scATAC-seq signal on cell
862   cycle genes in the 8 clusters. Clusters of cells predicted to be in cell cycle are indicated
863   with cell cycle icons. **(E)** Gene score heatmap of cluster 2 markers across all clusters. **(F)**
864   Gene score heatmap of the markers of cluster 2, also detected as IFNG-induced, G1-
865   phase-biased transcripts by bulk RNA-seq on Figure S4D. **(G)** Genome browser views on
866   *Cxcl9* and *Cxcl10*. Bulk ATAC- and RNAPII ChIP-seq signals in CTR, IFNG, IL-4-primed
867   and IL-4-primed and repolarized conditions (top part). scATAC-seq signal in the 8 clusters
868   (bottom part). Clusters of cells predicted to be in cell cycle are indicated with cell cycle
869   icons. **(H)** mRNA levels of *Irf8*, *Cxcl9* and *Cxcl10* in cell cycle across M0(CTR), M1(IFNG)
870   and M2rp(pIL-4+IFNG) conditions. On the bar graphs, significant changes were
871   determined by two tailed, unpaired t-test at p<0.05 (n=3). Shown are means with SDs. **(I)**
872   Percentage of macrophages in the G2/M phase of the cell cycle as determined by FACS.
873   Average of 3 experiments are used to calculate the percentage-wise distribution of cells
874   in G2/M relative to the highest value (M2p).
875

876   **Figure 7. Cycling macrophages upregulate a tissue regeneration gene program.**
877   **(A)** Scheme of the experimental setting. DEGs – differentially expressed genes, IPA –
878   Ingenuity Pathway Analysis. Heatmap represents differentially expressed genes across
879   the cell cycle phases in M0(CTR) macrophages. **(B)** Ingenuity Pathway Analysis of the
880   differentially expressed genes. Top 10 enriched biological functions are shown. **(C)**
881   Expression of a select set of genes from the first three enriched biological functions are
882   shown determined by bulk RNA-seq. **(D)** mRNA levels of *Fn1*, *Acta2* and *Col1a1*
883   measured by RT-qPCR. Significant changes were determined by two tailed, unpaired t-
884   test at p<0.05 (n=3). Shown are means with SDs. **(E)** UMAP projection of macrophages
885   from regenerating muscle, 2-, 3.5- and 5-days post-injury (DPI) determined by scRNA-
886   seq (GSE138826) (top). UMAP of the expression values of *Adgre1* (F4/80) (bottom). # -
887   normalized. **(F)** Violin plots represent gene expression of the indicated genes in single
888   macrophages on the different days (DPI) of regeneration (LogNormalized Expression).
889   **(G)** Feature scatter plots of the indicated gene pairs visualizing co-expression in single
890   macrophages (LogNormalized Expression). Single cells are colored by days post-injury

891 (DPI). Pearson correlation coefficients are indicated on each plot. **(H)** Loupe browser
892 images on spatial transcriptomics results in the stented wound healing model.
893 Hematoxylin and eosin (H&E) staining of the tissue is shown on top. Clusters defined
894 based on the expression programs of different tissue layers is shown below. Expression
895 levels of individual genes are depicted on the tissue slides and on the violin plots in the 7
896 clusters (Log$_2$ Expression values).
897
898
899 **Tables**
900 Table 1: Gene scores of the trajectory analysis of M2 macrophage polarization. Related
901 to Figure 1.
902 Table 2: Motif deviation scores of the trajectory analysis of M2 macrophage polarization.
903 Related to Figure 1.
904 Table 3: Gene scores of the trajectory analysis of M1 macrophage polarization. Related
905 to Figure 1.
906 Table 4: Motif deviation scores of the trajectory analysis of M1 macrophage polarization.
907 Related to Figure 1.
908 Table 5: Cluster-biased gene score values of polarized macrophages. Related to Figure
909 2.
910 Table 6: Marker genes of M1 and M2 macrophages determined by scRNA-seq. Related
911 to Figure S2B.
912 Table 7: Peak scores with transient, memory and primed kinetics. Related to Figure 5.
913 Table 8: Cluster-biased gene score values of repolarized macrophages. Related to Figure
914 6.
915 Table 9: Z-scores of cell cycle sensitive genes in M1 and M2 macrophages. Related to
916 Figure 4.
917 Table 10: Primer sequences used in this study.
918
919 **Methods**
920 **Bone marrow-derived macrophage culture**
921 Wild type, 2-3 months old female C57Bl6 mice were purchased from Jackson laboratories.
922 Mice were sacrificed and bone marrow was isolated form the tibiae and femora of the
923 animals. Red blood cell lysis was carried out and cells were plated in differentiation media
924 containing 10% FBS, Dulbecco's Modified Eagle's Medium (DMEM) and 20ng/ml mouse
925 M-CSF (Peprotech). On the third day of differentiation, media was replaced with fresh
926 differentiation media. Cytokine treatments sorting procedures were carried out on the 6th
927 day of differentiation.
928
929 **Treatment conditions**
930 Macrophages were treated with either IL-4 (20ng/ml) or IFNG (20ng/ml) (Peprotech). For
931 polarization we used 24 hours of IL-4 polarization and 3 hours of IFNG polarization in
932 differentiation media that contained 10% FBS, 1% penicillin/streptomycin and M-CSF
933 (20ng/ml). IL-4 priming was performed as follows: macrophages were polarized with IL-4
934 (20ng/ml) for 24 hours. Cell were washed three times with serum-free DMEM, then
935 differentiation media was replaced, and cells were rested for an additional 24 hours.
936 Repolarization was performed at this point for 3 hours with IFNG (20ng/ml). Macrophage

937 polarization for cell cycle experiments used 3 hours of polarization with either IL-4 or IFNG
938 (both at a 20ng/ml concentration).
939
940 **Fluorescence-activated cell sorting (FACS)**
941 Macrophages (~3 x 10^6) were stained with anti-F4/80 (rat monoclonal FITC-conjugated,
942 BioLegend) in a 1:200 dilution in FACS buffer for 20 minutes on ice. Cells were spun and
943 resuspended in serum-free DMEM pre-heated to 37C with Vybrant DyeCycle (1:500) and
944 incubated for 30 minutes at 37C followed by Propidium Iodide (PI) staining and sorting. PI
945 negative F4/80 positive macrophages were sorted from all three cell cycle stages
946 according to the Vybant DyeCycle signal.
947
948 **Real-time quantitative PCR for enhancer RNA and mRNA detection (qPCR)**
949 RNA was isolated with Trizol reagent (Ambion). RNA was reverse transcribed with High-
950 Capacity cDNA Reverse Transcription Kit (Applied Biosystems) according to the
951 manufacturer's instructions. Transcript quantification was performed by qPCR reactions
952 using SYBR green master mix (BioRad). Transcript levels were normalized to *Ppia*. Primer
953 sequences are available from Table S10.
954
955 **Chromatin immunoprecipitation sequencing (ChIP-seq)**
956 ChIP-seq was performed as previously described with minor modifications [1]. Bone
957 marrow-derived macrophages (3 x 10^6) were double crosslinked by 50mM DSG
958 (disuccinimidyl glutarate, #C1104 - ProteoChem) for 30 minutes followed by 10 minutes
959 of 1% formaldehyde. Formaldehyde was quenched by the addition of glycine. Nuclei were
960 isolated with ChIP lysis buffer (1% Triton x-100, 0.1% SDS, 150 mM NaCl, 1mM EDTA,
961 and 20 mM Tris, pH 8.0). Nuclei were sheared with Covaris sonicator using the following
962 setup: Fill level – 10, Duty Cycle – 5, PIP – 140, Cycles/Burst – 200, Time – 4 minutes).
963 Sheared chromatin was immunoprecipitated with RNAPIIpS2 antibody (Abcam - ab5095).
964 Antibody chromatin complexes were pulled down with Protein A magnetic beads and
965 washed once in IP wash buffer I. (1% Triton, 0.1% SDS, 150 mM NaCl, 1 mM EDTA, 20
966 mM Tris, pH 8.0, and 0.1% NaDOC), twice in IP wash buffer II. (1% Triton, 0.1% SDS,
967 500 mM NaCl, 1 mM EDTA, 20 mM Tris, pH 8.0, and 0.1% NaDOC), once in IP wash
968 buffer III. (0.25 M LiCl, 0.5% NP-40, 1mM EDTA, 20 mM Tris, pH 8.0, 0.5% NaDOC) and
969 once in TE buffer (10 mM EDTA and 200 mM Tris, pH 8.0). DNA was eluted from the
970 beads by vigorous shaking for 20 minutes in elution buffer (100mM $NaHCO_3$, 1% SDS).
971 DNA was decrosslinked overnight at 65C and purified with MinElute PCR purification kit
972 (Qiagen). DNA was quantified by Qubit and 10 ng DNA was used for sequencing library
973 construction with the Ovation Ultralow Library System V2 (Tecan) using 12 PCR cycles.
974 Libraries were sequenced on an Illumina Hiseq 2500 using paired-end 75bp reads.
975
976 **Bulk ATAC-seq and ChIP-seq computational methods**
977 Bulk epigenetics datasets were analyzed as described previously [2]. Briefly, reads were
978 trimmed for quality and adapter sequences using fastp. Trimmed reads were aligned to
979 the mm10 reference genome using hisat2. Aligned reads were deduplicated using picard.
980 Peaks were called for each sample using MACS2. A fixed-width, reproducible union peak
981 set for each group of samples (e.g., bulk ATAC-seq samples) was constructed by
982 iteratively merging individual peak calls for each sample and removing overlapping peaks
983 until a final, non-overlapping set of peaks was obtained. The union peak set was used to

984 create a sample by peak matrix. ATAC-seq coverage tracks were obtained by exporting
985 normalized bigwig files from R, normalized to reads in TSS, a gold-standard normalization
986 method that controls for both sequencing depth and library quality [3].
987
988 **Bulk RNA-seq**
989 Approximately 20ng total RNA was used for library preparation with Ovation Ultralow
990 RNA-seq V2 (Tecan) from two biological replicates. Libraries were generated according
991 to the manufacturer's instructions. Approximately 50ng amplified cDNA was subjected to
992 Ovation Ultralow V2 library generation and manufacturer's instructions were followed.
993 Libraries were size selected with E-Gel EX 2% agarose gels (Life Technologies) and
994 purified by QIAquick Gel Extraction Kit (Qiagen). Libraries were sequenced on HiSeq 2500
995 instrument.
996
997 **RNA-seq analysis**
998 Fastq files were pseudoaligned to a mm10 transcriptome index and the abundance of
999 transcripts was quantified using Kallisto v0.43.1 with bias correction [4]. The transcript-
1000 level abundance estimates were imported and summarized using tximport v1.16.1, and
1001 differential expression was determined using the DESeq2 package v1.28.11 in
1002 Bioconductor v.3.11. A gene was considered cell cycle-sensitive if it was differentially
1003 expressed between any two cell cycle stages in the control condition or the condition of
1004 interest (IL-4, or IFNG respectively) with an absolute fold change of ≥1.3 and a Benjamini–
1005 Hochberg adjusted p-value ≤0.001. If a gene was not differentially expressed between
1006 any two cell cycle stages with an adjusted p-value ≤0.001, it was considered cell cycle-
1007 insensitive. The cell cycle stage bias of a gene was assigned to the cell cycle stage where
1008 the gene showed the largest absolute scaled variance-stabilizing transformed expression.
1009
1010 **scATAC-seq sample and library generation**
1011 Single cell ATAC-seq experiments were performed on the 10x Chromium platform as
1012 described earlier [5]. Briefly, after cytokine treatments, macrophages were subjected to
1013 nuclei isolation according to the protocol of the manufacturer. Nuclei were counted and
1014 ~20,000 were submitted for tagmentation. After tagmentation, nuclei were loaded for
1015 capture using the 10x Chromium controller. After Gel emulsion generation, linear
1016 amplification was performed, followed by DNA purification following the manufacturer's
1017 protocol. The resulting DNA was used for library construction as described on the website
1018 of the manufacturer. Libraries were quantified by quantitative PCR and were sequenced
1019 on an Illumina Hiseq 2500 sequencer, using the following setup: 50bp read 1N, 8bp i7
1020 index, 16bp i5 index and 50bp read 2N. In this reaction, 1N and 2N refers to the DNA
1021 insert sequencing, while i5 and i7 sequencing identifies the individual barcodes of single
1022 cells.
1023
1024 **Single-cell RNA-seq library preparation**
1025 Single-cell RNA-seq libraries were prepared using the 10X Single Cell Immune Profiling
1026 Solution Kit (v1 Chemistry), according to the manufacturer's instructions. Briefly, FACS
1027 sorted cells were washed once with PBS + 0.04% BSA. Following reverse transcription
1028 and cell barcoding in droplets, emulsions were broken, and cDNA purified using
1029 Dynabeads MyOne SILANE followed by PCR amplification (98°C for 45 sec; 14 cycles of

1030 98°C for 20 sec, 67°C for 30 sec, 72°C for 1 min; 72°C for 1 min). For gene expression
1031 library construction, 50 ng of amplified cDNA was fragmented, and end-repaired, double-
1032 sided size selected with SPRIselect beads, PCR amplified with sample indexing primers
1033 (98°C for 45 sec; 14 cycles of 98°C for 20 sec, 54°C for 30 sec, 72°C for 20 sec; 72°C for
1034 1 min), and double-sided size selected with SPRIselect beads. Single-cell RNA libraries
1035 were sequenced on an Illumina HiSeq 4000 to a minimum sequencing depth of 25,000
1036 reads/cell using the read lengths 28bp Read1, 8bp i7 Index, 91bp Read2.
1037

1038 **scATAC-seq computational methods**
1039 scATAC-seq datasets were processed as described previously [6]. Briefly, reads were
1040 filtered, trimmed, and aligned to the mm10 reference genome using the 10X cellranger
1041 atac-count pipeline. Fragments files were loaded into ArchR for additional processing and
1042 analysis [7]. Separate ArchR projects were created for the three sample sets (priming,
1043 polarization, and repolarization) and additionally for each individual sample. Doublets
1044 were identified and removed using ArchR's default doublet simulation and calling
1045 procedures. Barcodes were removed that had an enrichment of Tn5 insertions in
1046 transcription start sites (TSS enrichment) less than 4 or less than 1000 fragments. Tiles
1047 and GeneScores matrices were computed by summing Tn5 insertions in predefined
1048 genomic windows. After clustering the cells, peaks were called by macs2 on
1049 pseudoreplicates sampled from each cluster to obtain a reproducible peak set retaining
1050 cell type specific peaks. Transcription factor motif deviations were computed using
1051 chromVar [8]. Imputation was performed using Magic [9]. Pseudo-bulk tracks for indicated
1052 groups of cells were exported from ArchR as bigwig files normalized by reads in
1053 transcription start sites. Tracks were visualized in the Integrative Genomics Viewer (IGV).
1054

1055 **scRNA-seq computational methods**
1056 Reads were filtered, trimmed, and aligned to the mm10 reference genome using the 10X
1057 cellranger count pipeline. Doublets were called for each sample individually using the R
1058 implementation of scrublet [10], rscrublet. Gene by barcode counts matrices were loaded
1059 into Seurat for additional processing and analysis [11]]. Separate Seurat objects were
1060 created for the three sample sets (priming, polarization, and repolarization) and for each
1061 individual sample. Barcodes with >12.5% mitochondrial reads, <200 unique features, or a
1062 scrublet score >0.25 were removed. Remaining cells were then clustered and visualized.
1063 Cell cycle phase predictions for each cell were performed following the vignette available
1064 online: https://satijalab.org/seurat/archive/v3.1/cell_cycle_vignette.html. Published
1065 datasets were also analyzed according to these standards.
1066

1067 **Statistical methods**
1068 Statistical analyses were performed in R or GraphPad Prism. qPCR measurements were
1069 presented as means +/- SD and three biological replicates were performed. The exact
1070 replicate numbers are indicated in the figure legends for each experiment. On the bar
1071 graphs, significant changes were determined by two tailed, unpaired t-test at $p<0.05$.
1072 Differential chromatin accessibility analyses across cell clusters were performed with the
1073 following parameters: FDR ≤ 0.01, Log_2 FC≥ 1.25, unless specified otherwise. Differential
1074 gene expression analyses of scRNA-seq results were performed with the following
1075 parameters: FDR≤ 0.01, FC≥ 1.3. Cell cycle phase-biased gene expression levels were

1076 determined as follows: Benjamini–Hochberg adjusted p-value ≤0.001; FC≥1.3 (two
1077 biological replicates were performed). Significant changes between the median peak
1078 scores of "Transient", "Memory" and "Primed" chromatin regions were determined by
1079 Wilcoxon Signed Rank Test, p<0.0001. Statistical parameters are reported in the figure
1080 legends and also in the results section.
1081

1082 **Data availability**
1083 Sequencing data has been deposited to GEO under accession: GSE178526
1084 Token for accessing the data: qrmtekckjjuxngd
1085 Published data that has been used in this study: GSE138826, GSE84520.
1086

1087

1088 **References**

1089 1.   Lavin, Y., et al., *Tissue-resident macrophage enhancer landscapes are shaped*
1090   *by the local microenvironment.* Cell, 2014. **159**(6): p. 1312-26.
1091 2.   Gosselin, D., et al., *Environment Drives Selection and Function of Enhancers*
1092   *Controlling Tissue-Specific Macrophage Identities.* Cell, 2014. **159**(6): p. 1327-
1093   1340.
1094 3.   Bleriot, C., S. Chakarov, and F. Ginhoux, *Determinants of Resident Tissue*
1095   *Macrophage Identity and Function.* Immunity, 2020. **52**(6): p. 957-970.
1096 4.   Guilliams, M. and F.R. Svedberg, *Does tissue imprinting restrict macrophage*
1097   *plasticity?* Nat Immunol, 2021. **22**(2): p. 118-127.
1098 5.   Roberts, R.A., et al., *Role of the Kupffer cell in mediating hepatic toxicity and*
1099   *carcinogenesis.* Toxicol Sci, 2007. **96**(1): p. 2-15.
1100 6.   Mould, K.J., et al., *Single cell RNA sequencing identifies unique inflammatory*
1101   *airspace macrophage subsets.* JCI Insight, 2019. **4**(5).
1102 7.   Saliba, A.E., et al., *Single-cell RNA-seq ties macrophage polarization to growth*
1103   *rate of intracellular Salmonella.* Nat Microbiol, 2016. **2**: p. 16206.
1104 8.   Cochain, C., et al., *Single-Cell RNA-Seq Reveals the Transcriptional Landscape*
1105   *and Heterogeneity of Aortic Macrophages in Murine Atherosclerosis.* Circ Res,
1106   2018. **122**(12): p. 1661-1674.
1107 9.   Draijer, C., L.R.K. Penke, and M. Peters-Golden, *Distinctive Effects of GM-CSF*
1108   *and M-CSF on Proliferation and Polarization of Two Major Pulmonary*
1109   *Macrophage Populations.* J Immunol, 2019. **202**(9): p. 2700-2709.
1110 10.   Otero, K., et al., *Macrophage colony-stimulating factor induces the proliferation*
1111   *and survival of macrophages via a pathway involving DAP12 and beta-catenin.*
1112   Nat Immunol, 2009. **10**(7): p. 734-43.
1113 11.   Sinha, S.K., et al., *Local M-CSF (Macrophage Colony-Stimulating Factor)*
1114   *Expression Regulates Macrophage Proliferation and Apoptosis in*
1115   *Atherosclerosis.* Arterioscler Thromb Vasc Biol, 2021. **41**(1): p. 220-233.
1116 12.   Jenkins, S.J., et al., *Local macrophage proliferation, rather than recruitment from*
1117   *the blood, is a signature of TH2 inflammation.* Science, 2011. **332**(6035): p. 1284-
1118   8.
1119 13.   Jarjour, N.N., et al., *Bhlhe40 mediates tissue-specific control of macrophage*
1120   *proliferation in homeostasis and type 2 immunity.* Nat Immunol, 2019. **20**(6): p.
1121   687-700.

1122   14.   Bleriot, C., et al., *Liver-resident macrophage necroptosis orchestrates type 1*
1123   *microbicidal inflammation and type-2-mediated tissue repair during bacterial*
1124   *infection.* Immunity, 2015. **42**(1): p. 145-58.
1125   15.   Wynn, T.A. and K.M. Vannella, *Macrophages in Tissue Repair, Regeneration,*
1126   *and Fibrosis.* Immunity, 2016. **44**(3): p. 450-462.
1127   16.   Chazaud, B., *Inflammation and Skeletal Muscle Regeneration: Leave It to the*
1128   *Macrophages!* Trends Immunol, 2020. **41**(6): p. 481-492.
1129   17.   Zhu, B., et al., *Uncoupling of macrophage inflammation from self-renewal*
1130   *modulates host recovery from respiratory viral infection.* Immunity, 2021.
1131   18.   Van Dyken, S.J. and R.M. Locksley, *Interleukin-4- and interleukin-13-mediated*
1132   *alternatively activated macrophages: roles in homeostasis and disease.* Annu
1133   Rev Immunol, 2013. **31**: p. 317-43.
1134   19.   Murray, P.J., et al., *Macrophage activation and polarization: nomenclature and*
1135   *experimental guidelines.* Immunity, 2014. **41**(1): p. 14-20.
1136   20.   Murray, P.J., *Macrophage Polarization.* Annu Rev Physiol, 2017. **79**: p. 541-566.
1137   21.   Orecchioni, M., et al., *Macrophage Polarization: Different Gene Signatures in*
1138   *M1(LPS+) vs. Classically and M2(LPS-) vs. Alternatively Activated Macrophages.*
1139   Front Immunol, 2019. **10**: p. 1084.
1140   22.   Ostuni, R., et al., *Latent enhancers activated by stimulation in differentiated cells.*
1141   Cell, 2013. **152**(1-2): p. 157-71.
1142   23.   Czimmerer, Z., et al., *The Transcription Factor STAT6 Mediates Direct*
1143   *Repression of Inflammatory Enhancers and Limits Activation of Alternatively*
1144   *Polarized Macrophages.* Immunity, 2018. **48**(1): p. 75-90 e6.
1145   24.   Kang, K., et al., *Interferon-gamma Represses M2 Gene Expression in Human*
1146   *Macrophages by Disassembling Enhancers Bound by the Transcription Factor*
1147   *MAF.* Immunity, 2017. **47**(2): p. 235-250 e4.
1148   25.   Kaikkonen, M.U., et al., *Remodeling of the enhancer landscape during*
1149   *macrophage activation is coupled to enhancer transcription.* Mol Cell, 2013.
1150   **51**(3): p. 310-25.
1151   26.   Qiao, Y., et al., *Synergistic activation of inflammatory cytokine genes by*
1152   *interferon-gamma-induced chromatin remodeling and toll-like receptor signaling.*
1153   Immunity, 2013. **39**(3): p. 454-69.
1154   27.   Park, S.H., et al., *Type I interferons and the cytokine TNF cooperatively*
1155   *reprogram the macrophage epigenome to promote inflammatory activation.* Nat
1156   Immunol, 2017. **18**(10): p. 1104-1116.
1157   28.   Daniel, B., et al., *The Nuclear Receptor PPARgamma Controls Progressive*
1158   *Macrophage Polarization as a Ligand-Insensitive Epigenomic Ratchet of*
1159   *Transcriptional Memory.* Immunity, 2018. **49**(4): p. 615-626 e6.
1160   29.   Piccolo, V., et al., *Opposing macrophage polarization programs show extensive*
1161   *epigenomic and transcriptional cross-talk.* Nat Immunol, 2017. **18**(5): p. 530-540.
1162   30.   Daniel, B., et al., *The transcription factor EGR2 is the molecular linchpin*
1163   *connecting STAT6 activation to the late, stable epigenomic program of alternative*
1164   *macrophage polarization.* Genes Dev, 2020. **34**(21-22): p. 1474-1492.
1165   31.   Satpathy, A.T., et al., *Massively parallel single-cell chromatin landscapes of*
1166   *human immune cell development and intratumoral T cell exhaustion.* Nat
1167   Biotechnol, 2019. **37**(8): p. 925-936.

1168   32.   Granja, J.M., et al., *ArchR is a scalable software package for integrative single-*
1169   *cell chromatin accessibility analysis.* Nat Genet, 2021. **53**(3): p. 403-411.
1170   33.   Tirosh, I., et al., *Dissecting the multicellular ecosystem of metastatic melanoma*
1171   *by single-cell RNA-seq.* Science, 2016. **352**(6282): p. 189-96.
1172   34.   Langlais, D., L.B. Barreiro, and P. Gros, *The macrophage IRF8/IRF1 regulome is*
1173   *required for protection against infections and is associated with chronic*
1174   *inflammation.* J Exp Med, 2016. **213**(4): p. 585-603.
1175   35.   Nasser, H., et al., *Establishment of bone marrow-derived M-CSF receptor-*
1176   *dependent self-renewing macrophages.* Cell Death Discov, 2020. **6**: p. 63.
1177   36.   Xie, B., et al., *Reconstitution and characterization of the human DNA polymerase*
1178   *delta four-subunit holoenzyme.* Biochemistry, 2002. **41**(44): p. 13133-42.
1179   37.   Xaus, J., et al., *Interferon gamma induces the expression of p21waf-1 and arrests*
1180   *macrophage cell cycle, preventing induction of apoptosis.* Immunity, 1999. **11**(1):
1181   p. 103-13.
1182   38.   Ruckerl, D. and J.E. Allen, *Macrophage proliferation, provenance, and plasticity in*
1183   *macroparasite infection.* Immunol Rev, 2014. **262**(1): p. 113-33.
1184   39.   van Kooyk, Y., J.M. Ilarregui, and S.J. van Vliet, *Novel insights into the*
1185   *immunomodulatory role of the dendritic cell and macrophage-expressed C-type*
1186   *lectin MGL.* Immunobiology, 2015. **220**(2): p. 185-92.
1187   40.   Roszer, T., *Understanding the Mysterious M2 Macrophage through Activation*
1188   *Markers and Effector Mechanisms.* Mediators Inflamm, 2015. **2015**: p. 816460.
1189   41.   Hah, N., et al., *A rapid, extensive, and transient transcriptional response to*
1190   *estrogen signaling in breast cancer cells.* Cell, 2011. **145**(4): p. 622-34.
1191   42.   Daniel, B., et al., *The active enhancer network operated by liganded RXR*
1192   *supports angiogenic activity in macrophages.* Genes Dev, 2014. **28**(14): p. 1562-
1193   77.
1194   43.   Liu, S.X., et al., *Trajectory analysis quantifies transcriptional plasticity during*
1195   *macrophage polarization.* Sci Rep, 2020. **10**(1): p. 12273.
1196   44.   Arnold, L., et al., *Inflammatory monocytes recruited after skeletal muscle injury*
1197   *switch into antiinflammatory macrophages to support myogenesis.* J Exp Med,
1198   2007. **204**(5): p. 1057-69.
1199   45.   Martinez, C.O., et al., *Regulation of skeletal muscle regeneration by CCR2-*
1200   *activating chemokines is directly related to macrophage recruitment.* Am J Physiol
1201   Regul Integr Comp Physiol, 2010. **299**(3): p. R832-42.
1202   46.   Ochoa, O., et al., *Delayed angiogenesis and VEGF production in CCR2-/- mice*
1203   *during impaired skeletal muscle regeneration.* Am J Physiol Regul Integr Comp
1204   Physiol, 2007. **293**(2): p. R651-61.
1205   47.   Oprescu, S.N., et al., *Temporal Dynamics and Heterogeneity of Cell Populations*
1206   *during Skeletal Muscle Regeneration.* iScience, 2020. **23**(4): p. 100993.
1207   48.   Wheeler, J.R., et al., *RNA-Binding Proteins Direct Myogenic Cell Fate Decisions.*
1208   bioRxiv, 2021.
1209   49.   Foster, D.S., et al., *Integrated spatial multi-omics reveals fibroblast fate during*
1210   *tissue repair.* bioRxiv, 2021.
1211   50.   Cheng, S., et al., *A pan-cancer single-cell transcriptional atlas of tumor infiltrating*
1212   *myeloid cells.* Cell, 2021. **184**(3): p. 792-809 e23.
1213   51.   Grant, R.A., et al., *Circuits between infected macrophages and T cells in SARS-*
1214   *CoV-2 pneumonia.* Nature, 2021. **590**(7847): p. 635-641.

1215 52. Sarvari, A.K., et al., *Plasticity of Epididymal Adipose Tissue in Response to Diet-*
1216   *Induced Obesity at Single-Nucleus Resolution.* Cell Metab, 2021. **33**(2): p. 437-
1217   453 e5.
1218 53. Lin, J.D., et al., *Single-cell analysis of fate-mapped macrophages reveals*
1219   *heterogeneity, including stem-like properties, during atherosclerosis progression*
1220   *and regression.* JCI Insight, 2019. **4**(4).
1221 54. Luecken, M.D. and F.J. Theis, *Current best practices in single-cell RNA-seq*
1222   *analysis: a tutorial.* Mol Syst Biol, 2019. **15**(6): p. e8746.
1223 55. Munoz-Rojas, A.R., et al., *Co-stimulation with opposing macrophage polarization*
1224   *cues leads to orthogonal secretion programs in individual cells.* Nat Commun,
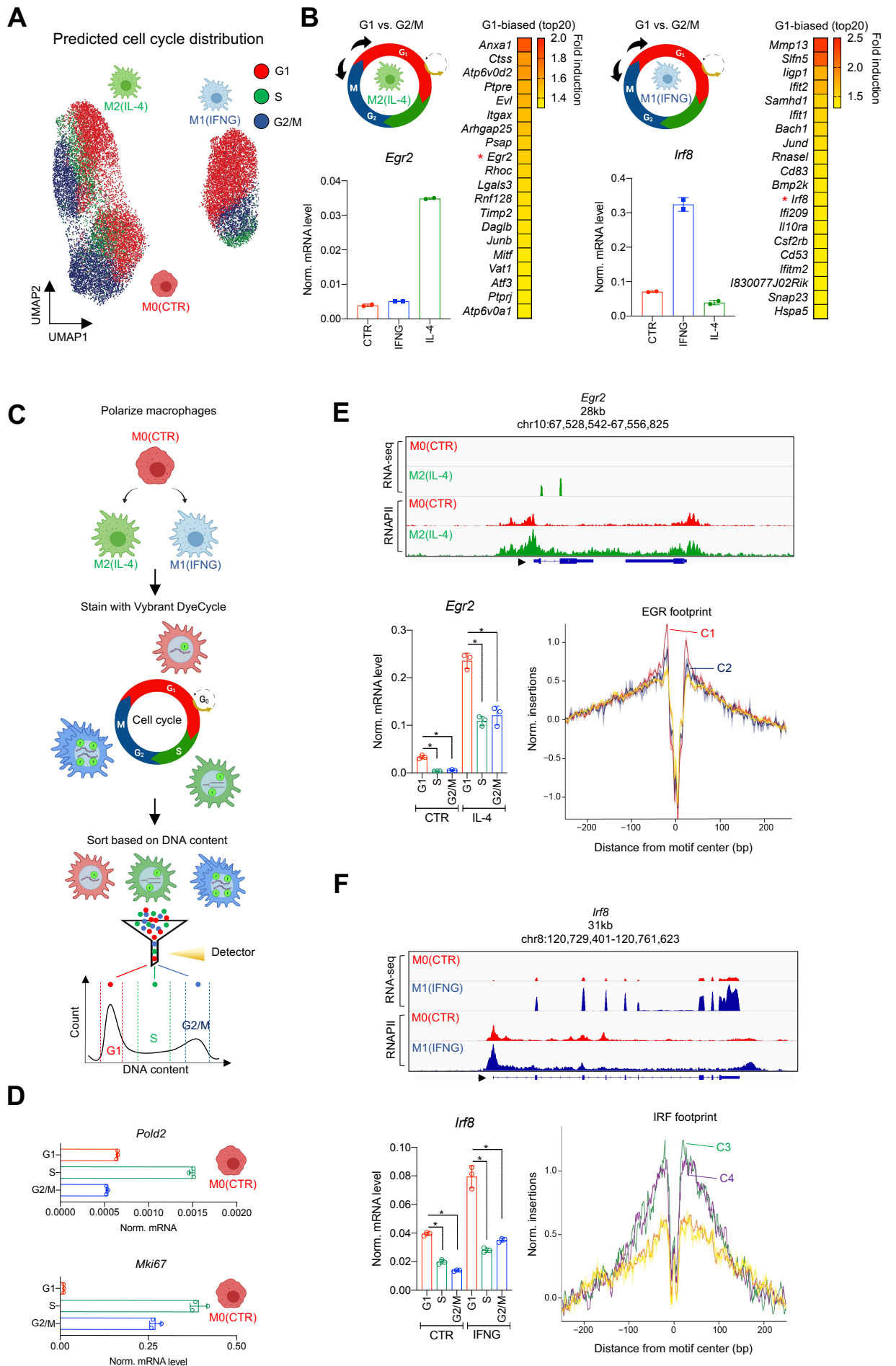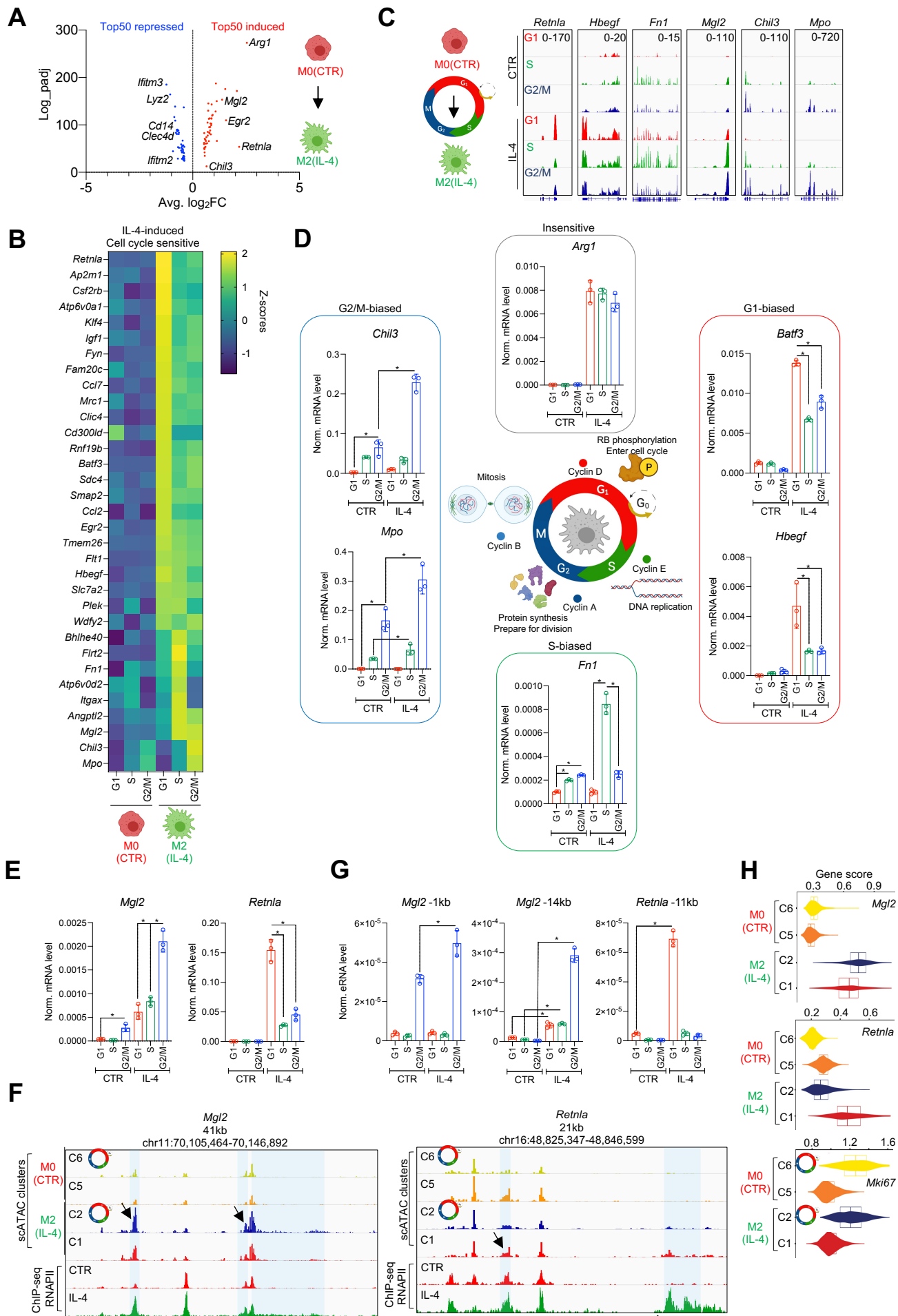1225   2021. **12**(1): p. 301.
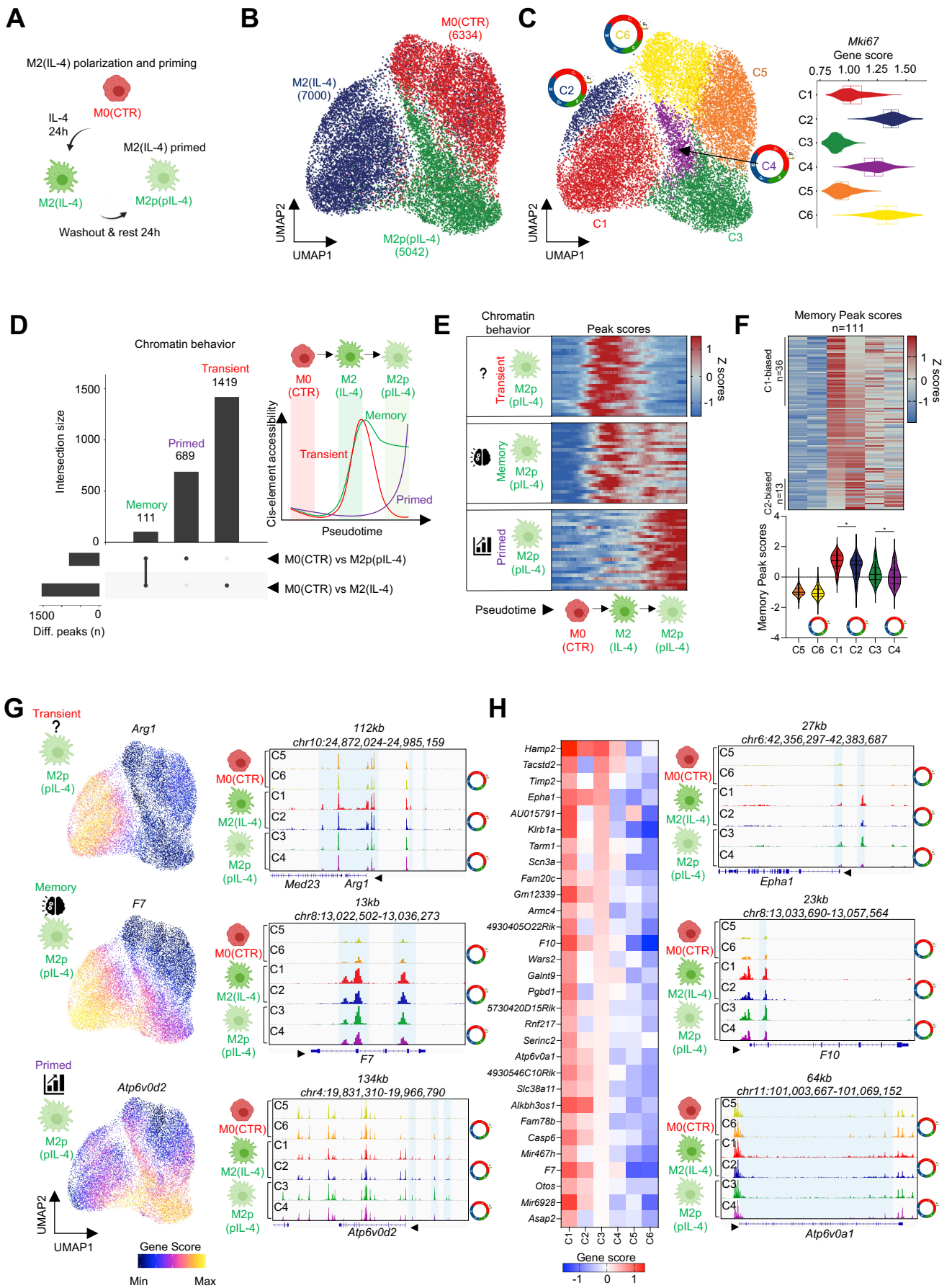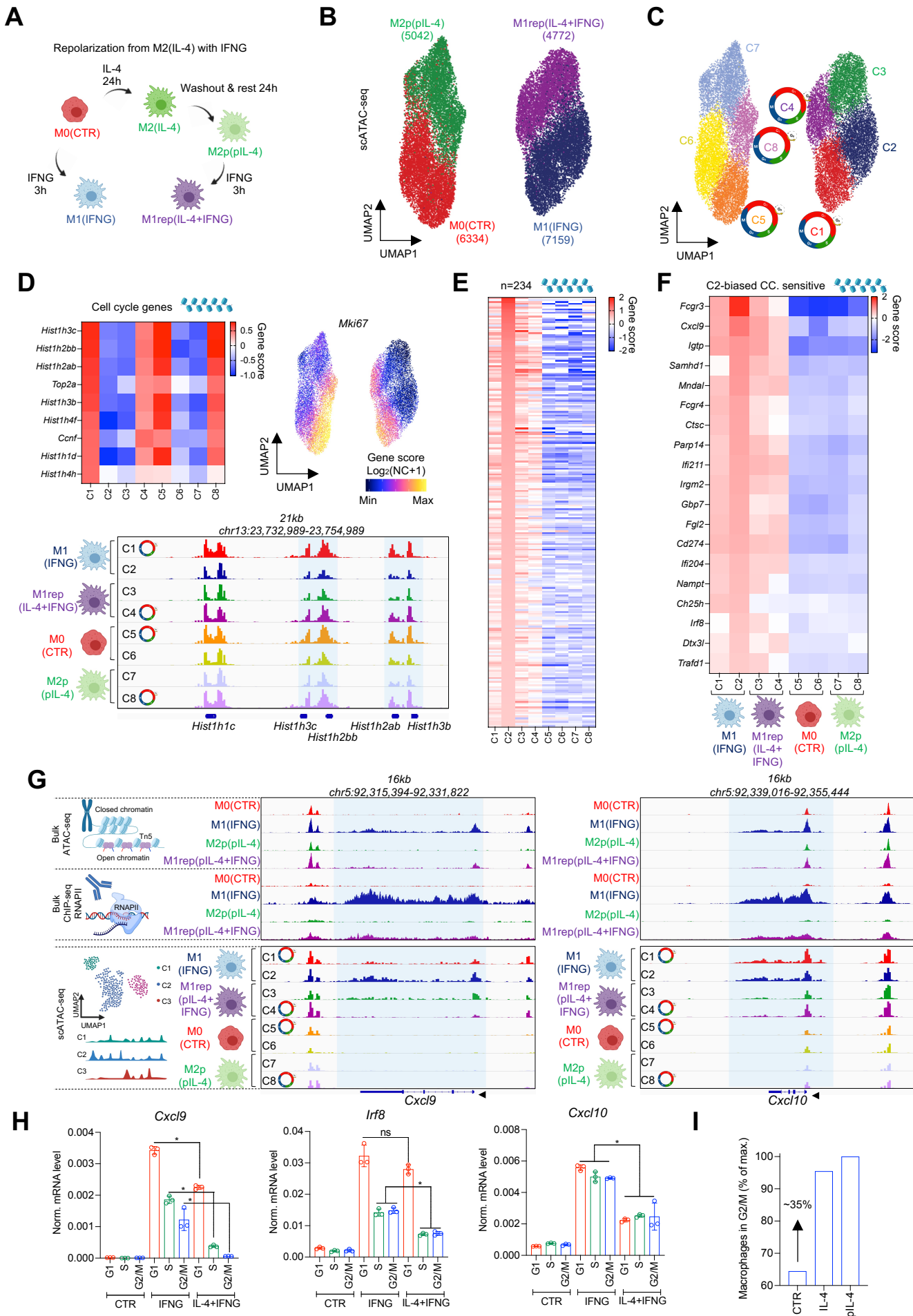
Figure 1.
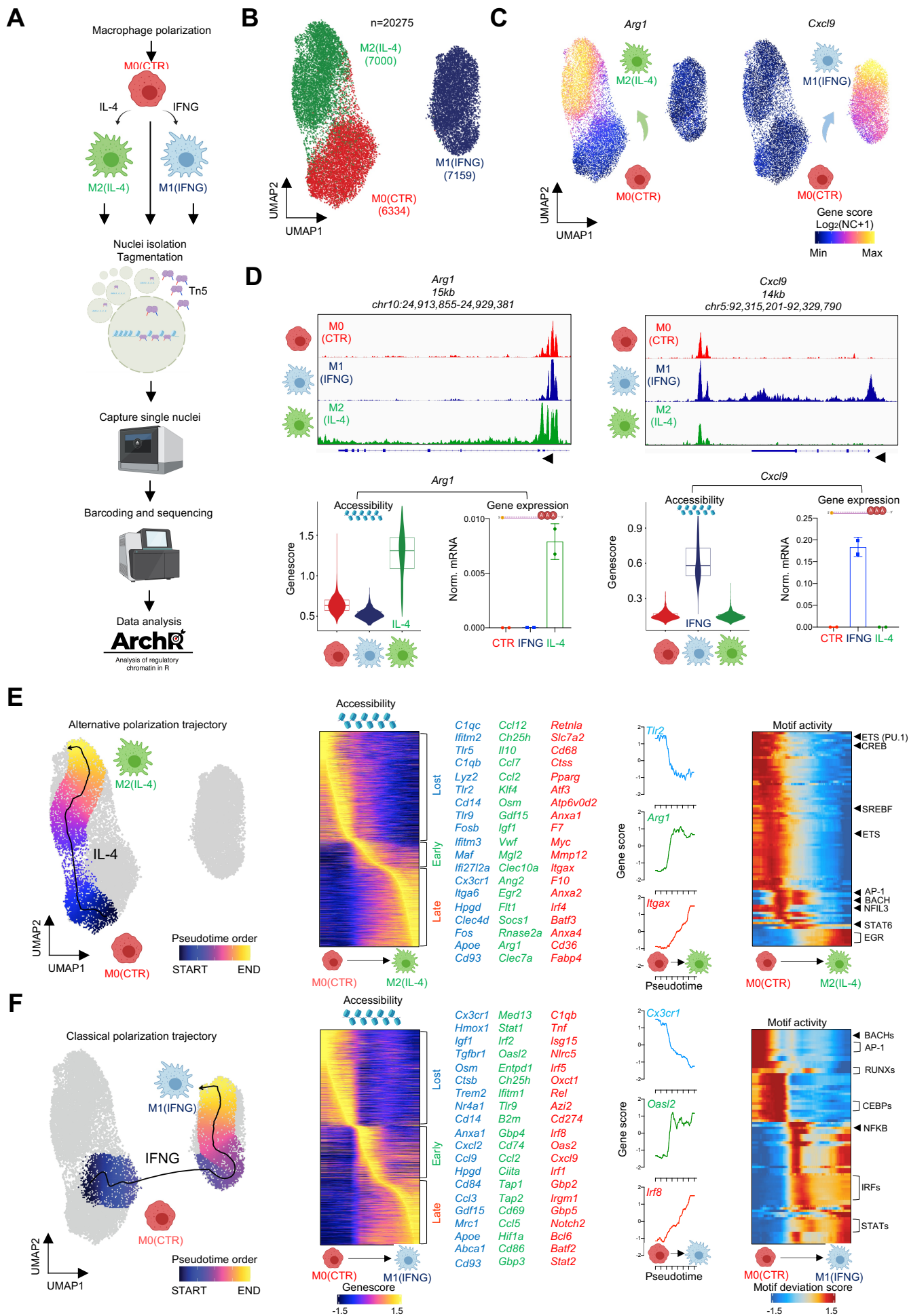
Figure 2.
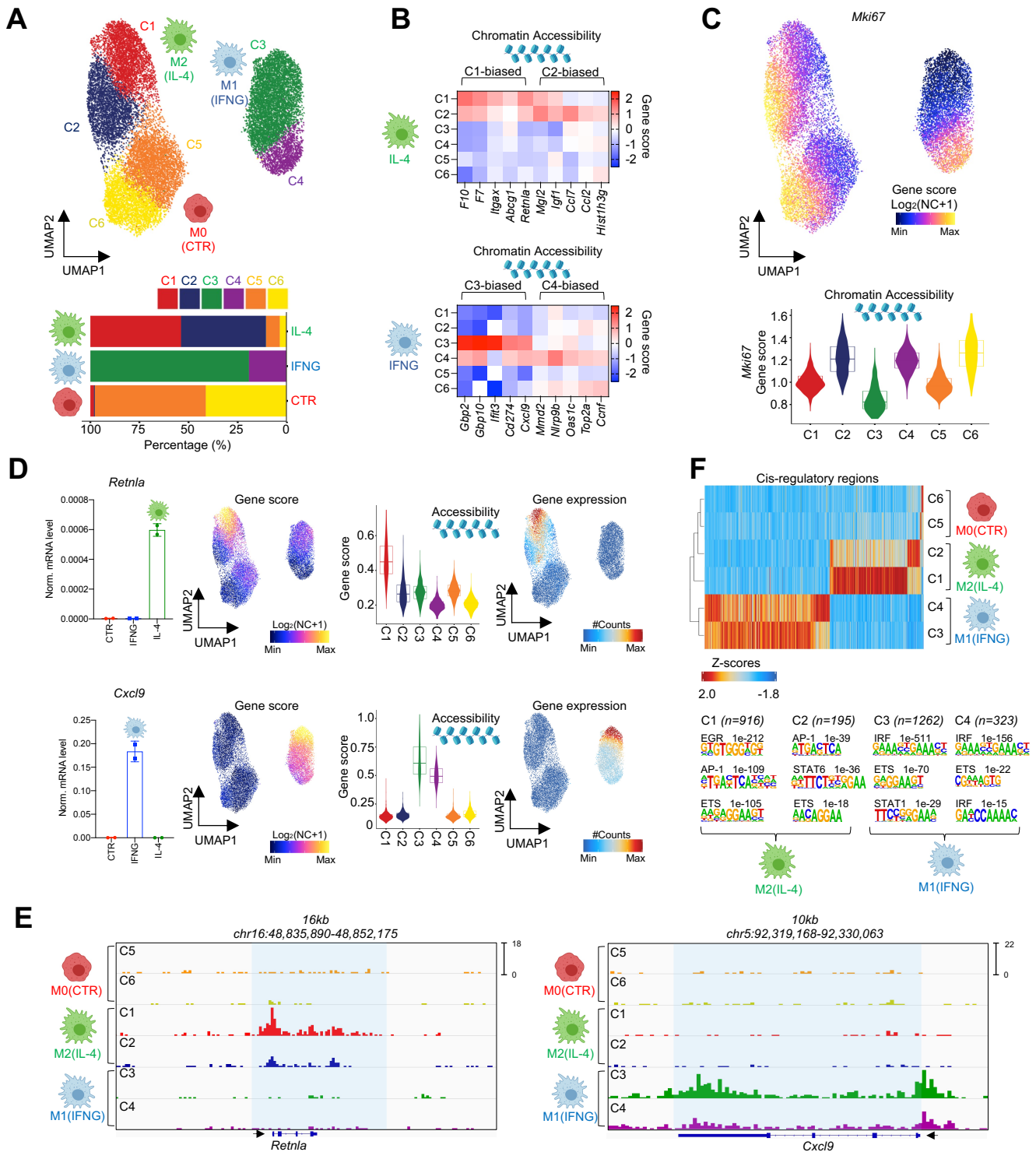
Figure 3.

Figure 4.

Figure 5.

Figure 6.

Figure 7.